SKIM-MPRC TN-5:
Estimation of Non-Geophysical Doppler and Wave Doppler, and inversion algorithm for SKIM

Submitted by:

LOPS, France

Customer	ESA
Author	LOPS
ESA ITT Number	4000124664/18/NL/NA
Document Reference	SKIM-MPRC_LOPS_2019
SoW Reference	ESA-EOPSM-SKIM-SOW-3262
Version/Revision	1.0
Date of issue	April 29, 2019

Issued by (LOPS)	Fabrice Ardhuin, Louis Marié, Charles Peureux, Jean-Marc Delouis, Victor Gressani	2019/04/29	
Reviewed by (LOPS)	Bertrand Chapron		
		2019/04/29	Date and signature
Approved by (ESA)	Craig Donlon		

Chronology			
Issue	**Date**	**Change record**	**Author**
0.1	2019/04/14	Initial document	F. Ardhuin
1.0	2019/04/29	Finalized and delivered	F. Ardhuin

Contents

1 Introduction

This document gives an overview of a processing chain from the SKIM L1B to L2B products, particularly to estimate and subtract the nongeophysical Doppler U_{NG}, and split U_{GD} into $U_{CD} + U_{WD}$. Beyond this technical goal, we also wish to highlight the limitations and perspectives of the present work, revealing how SKIM really works. In particular,

- SKIM measurements of Doppler are based on the detection of a radar signal, associated to ocean surface slopes, that have a Doppler signature due to the correlation of slopes and velocities at the ocean surface. Hence the geophysical parameter at the heart of the measurement is the mean slope velocity vector, which is imaged via tilt and range bunching mechanisms similar to those on SWIM.

- SKIM data can be processed in a range-resolved mode (as described in this document), but it may just as well be processed in Fourier space (following the Delta-K idea) because so far we have not used the range-resolved data to say something about ocean properties attached to sub-footprint locations: we are not considering SKIM as a 1D-along-range-imager (this could be interesting for nearshore applications, rivers ...).

- The high directional sensitivity of the range-resolved measurements, using the principle of the wave spectrometer (Jackson et al., 1985; Jackson, 1987), as beautifully revealed by SWIM data, is both a strength and a weakness. This is because of the different directionalities of the signals in σ^0, Doppler and wave modulations. Indeed, some wave components, propagating close to the along-track direction, may not be directly recovered. Hence we never get a full directional spectrum in a "box" that does not include the center of the swath. This may be problematic if the wave field has strong gradients at scales less than 100 km, either due to proximity to the coast or ice edge, or due to strong currents (Ardhuin et al., 2017; Quilfen and Chapron, 2019). The "Doppler Beam Sharpening" can be used to "blur" this directional selectivity (by reducing the azimuthal integration L_y) while at the same time reducing the noise floor and speckle of wave spectra. A compromise between errors due to spatial gradients and errors due to less accurate proxy parameters is at the heart of the difference between the two approaches proposed to split U_{GD} in $U_{CD} + U_{WD}$.

- The strength of this highly sensitive directional measurements, for wave components away from the along-track direction, their spatial gradients are very well captured. There is thus room to more directly use these measurements to enable data-driven methods (and this is where AI capability may help to identify analogs and related patterns) about the waves in other (not imaged) directions. This appears like re-discovering a parametric spectral shape, but more properly taking into account all the effects that put the sea-state in non-equilibrium: the space and time history (including rotation) of the wind field, the presence of swell systems, seasonal and regional changes of the ocean-atmosphere dynamics. A great opportunity is to measure spectrally-resolved quantities, with different relaxation space and time scales. This should be used much better, in particular as we are measuring the main forcing effects of the waves: the wind and current. Maybe the only missing piece of information in the time history of the wind (i.e. the wind vector a few hours before), but a good proxy for this may be the change in direction as a function of frequency within the wind sea partition. Basically, a relatively narrow angle window (say 2 non-contiguous $40°$ sectors as shown in figure 30) may be enough to "extrapolate" the shape of the wave spectrum outside of that window. Besides, if U_{WD} has, like the radial Stokes drift, an azimuth variation of the form $M_{WD} \cos(\varphi - \varphi_{WD})$, then the details of the directional distribution do not matter, and the first azimuth moments a_1 and b_1 (Kuik et al., 1988) are enough.

- Most of the analysis is based on a forward numerical model that may be biased, i.e. the M_{WD} predicted in figure 25 is apparently 30 to 50% above the values measured by Yurovsky et al. (2017). If the latter is correct, this can be due to a poor representation of wave properties, both in the range of resolved wavenumbers with a too high energy level for $f > 0.4$ Hz (Stopa et al., 2016), and inadequate directional distribution at frequencies above 2 to 3 times the wind sea peak frequency (Peureux and Ardhuin, 2016). It can also come from errors in the parameterized high frequency tail (for $f > 0.7$ Hz) beyond the range resolved by the model (Elfouhaily et al., 1997; Peureux et al., 2018). This is the first step in a seamless combination of a numerical wave model and a "remote sensing compatible" parametric tail for the high frequencies. The sensitivity to various sea state parameters appears

realistic, in line with the KaDop algorithm of Yurovsky et al. (2019), so that the relative variations of U_{WD} and M_{WD} are meaningful and we can add a near-constant local wind-sea contribution $U_{\mathrm{WD,ws}}$ to a non-local swell contribution to $U_{\mathrm{WD,swell}}$.

- Related to the previous issue, the SWIM data reveals interesting patterns of σ^0, consistent with previous GPM data, that is generally well represented by the forward model. We may thus rely on the the patterns of σ^0 variation as a function of incidence and azimuth and sea state to guide a SKIM inversion, keeping in mind that the forward model has some biases. In this respect, it is reassuring that the underlying numerical wave model (used for the long waves) was built with the purpose of representing the variability of long wave mean square slopes (Ardhuin et al., 2010; Stopa et al., 2016) that have measurable effects on near-nadir Ku- and Ka-band σ^0 (Tran et al., 2007; Nouguier et al., 2018; Yan et al., 2019).

The present document is thus not the final word on how to use SKIM data to best retrieve current vectors and wave spectra.

1.1 Geophysical and non-geophysical Doppler

We recall that the particularity of the SKIM Doppler measurement is the tight combination of non-geophysical Doppler components associated to the exact knowledge of the platform-to-ocean velocity (V_x, V_x, V_y) that gives a non-geophysical contribution V_{NG}. This issue is very well covered by Rodriguez Rodríguez et al. (2018). We call V_{NG} "non-geophysical" because this velocity is not geophysical, i.e. it applies to a frozen-homogeneous surface. Yet, as it will be discussed it may contain some geophysical effects, likely associated to a non-uniform surface scene (varying topography and/or backscatter coefficient).
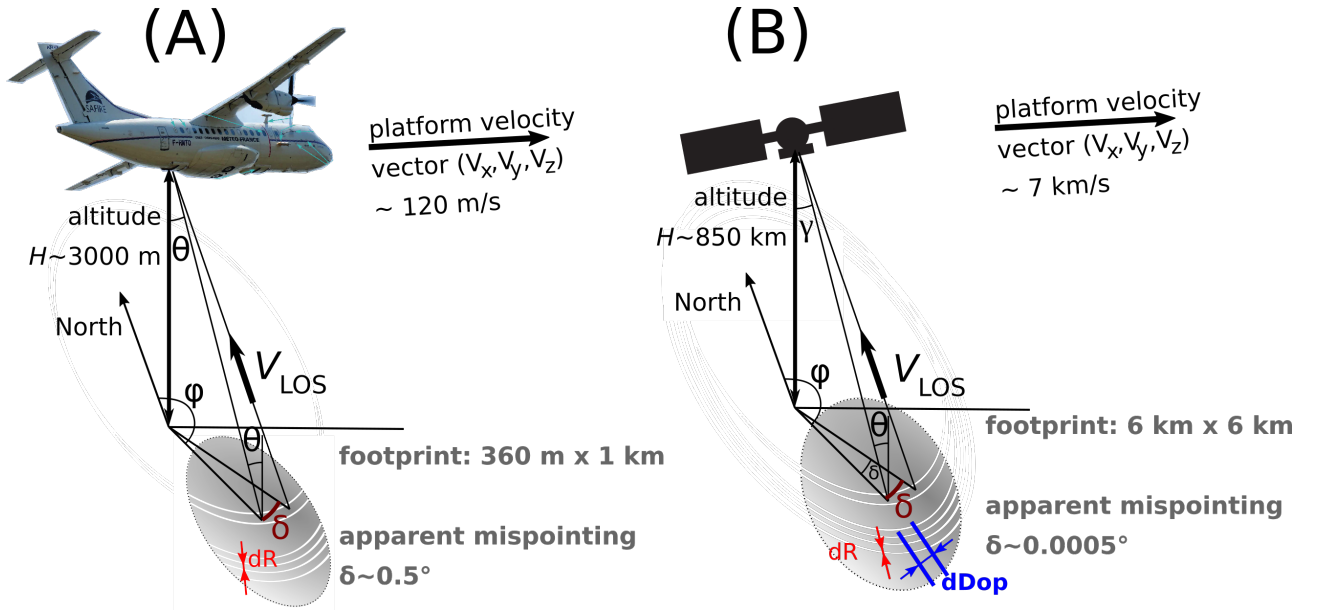

Figure 1: (A) Schematic of ATR-42 and KuROS instrument and definition of viewing angles, azimuth φ and incidence θ, and (B) comparison with the SKIM viewing geometry for which the elevation angle γ is slightly different from the incidence angle, mainly due to the Earth sphericity. A variation of surface backscatter across the footprint and as a function of azimuth φ is represented by the grey shading, and gives an apparent mispointing δ. In KuROS data, each measurement is integrated in azimuth across the antenna lobe. In the case of SKIM, the use of unfocused SAR allows the separation of echoes in the azimuth direction with a resolution of the order of 300 m. The apparent mis-pointing is much smaller for SKIM because of a smaller antenna aperture and a more uniform radar backscatter at the scale of the footprint.

Accordingly, we consider

$$U_{GD} = (V_{\text{LOS}} - V_{NG})/\sin\theta. \tag{1}$$

The residual velocity is then called the geophysical Doppler velocity U_{GD} because it only contains geophysical velocity effects, associated to ocean waves and currents. As understood, e.g. (Mouche et al., 2008; Nouguier et al., 2018), this velocity corresponds to the motion of detected scatters in a way that is very sensitive of the imaging mechanism, radar properties and processing. SKIM is a near-nadir instrument, operating at high-frequency and the scattering mechanism closely approaches optical measurements as largely dominated by non-polarized specular and quasi-specular scatters (Walsh et al., 1998; Vandemark et al., 2004; Walsh et al., 2008; Nouguier et al., 2016).
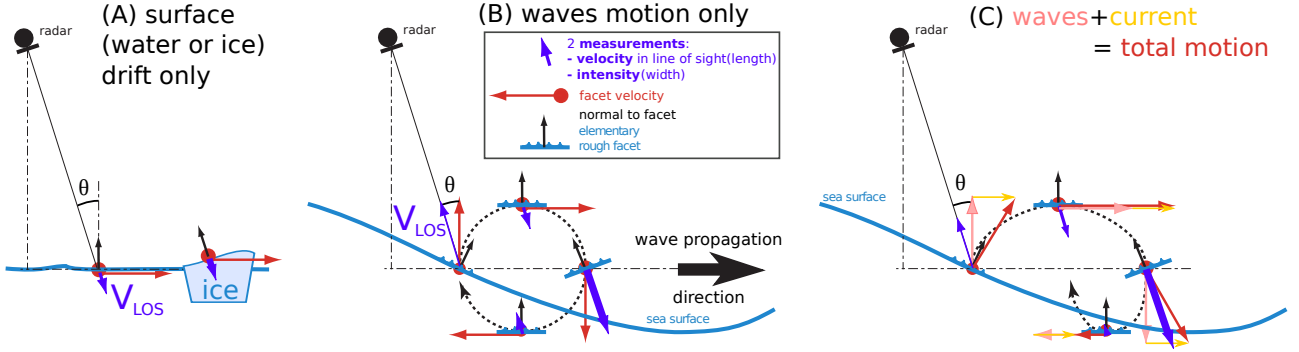
Figure 2: Schematic of (A) ice drift, (B) wave and (C) wave and current contributions to Doppler velocities at the scale of elementary facets. These are averaged into a radar pixel, so that sub-pixel waves contribute a mean velocity due to the correlation of surface slopes and velocities in the wave field.

1.2 Contributions to the Geophysical Doppler

Except for the case of sea ice drift, to be discussed in a later version, at a facet level, the surface is moving because (an ensemble of) waves are moving it. For a perfect sine wave of period T propagating over deep water, the phase speed of the wave is

$$C = \frac{gT}{2\pi} + U\cos(\varphi_w - \varphi_U) \tag{2}$$

where U is the current speed, φ_w is the wave propagation azimuth direction, and φ_U is the current direction. This is the principle of the coastal HF radars (Barrick et al., 1974; Stewart and Joy, 1974) that select a pair of sine wave components via a very selective Bragg scattering mechanism at grazing angles.

In the case of SKIM, or other systems (e.g. SAR systems) for which the backscatter is not selecting a single wavenumber on the sea surface, a superposition of waves shall contribute. We get a compound mixture of C's, and the different terms become (Nouguier et al., 2018; Yurovsky et al., 2019),

$$C \quad \rightarrow \quad U_{GD} \tag{3}$$

$$\frac{gT}{2\pi} \quad \rightarrow \quad U_{WD} \tag{4}$$

$$U \quad \rightarrow \quad U_{CD} \tag{5}$$

where the current U sampled at depth $k/4\pi$ (Stewart and Joy, 1974) for a monochromatic sine wave, is now a weighted average U_{CD} of the currents at different depths, where the weighting function is determined by the wave slope spectrum. Indeed, the velocity U_{GD} integrates the velocity of the tilted-facets on the ocean surface. Within facets, quasi-specular and specular points are selected, further modulated by the local directional tilts $\nabla\eta$, leading to a modulated averaged intensity and a weighted velocity as

$$\sigma^0 \quad = \quad \int \sigma(\nabla\eta) P(\nabla\eta) d\nabla\eta \tag{6}$$

$$\sigma^0 * V_{LOS} \quad = \quad \int V_{LOS}(\nabla\eta)\sigma(\nabla\eta)P(\nabla\eta)d\nabla\eta \tag{7}$$

with $\sigma(\nabla\eta)$ an individual local radar cross section, corresponding to a tilted facet, with a local line-of-sight velocity V_{LOS}, and $P(\nabla\eta)$ the facet-tilt probability distribution.
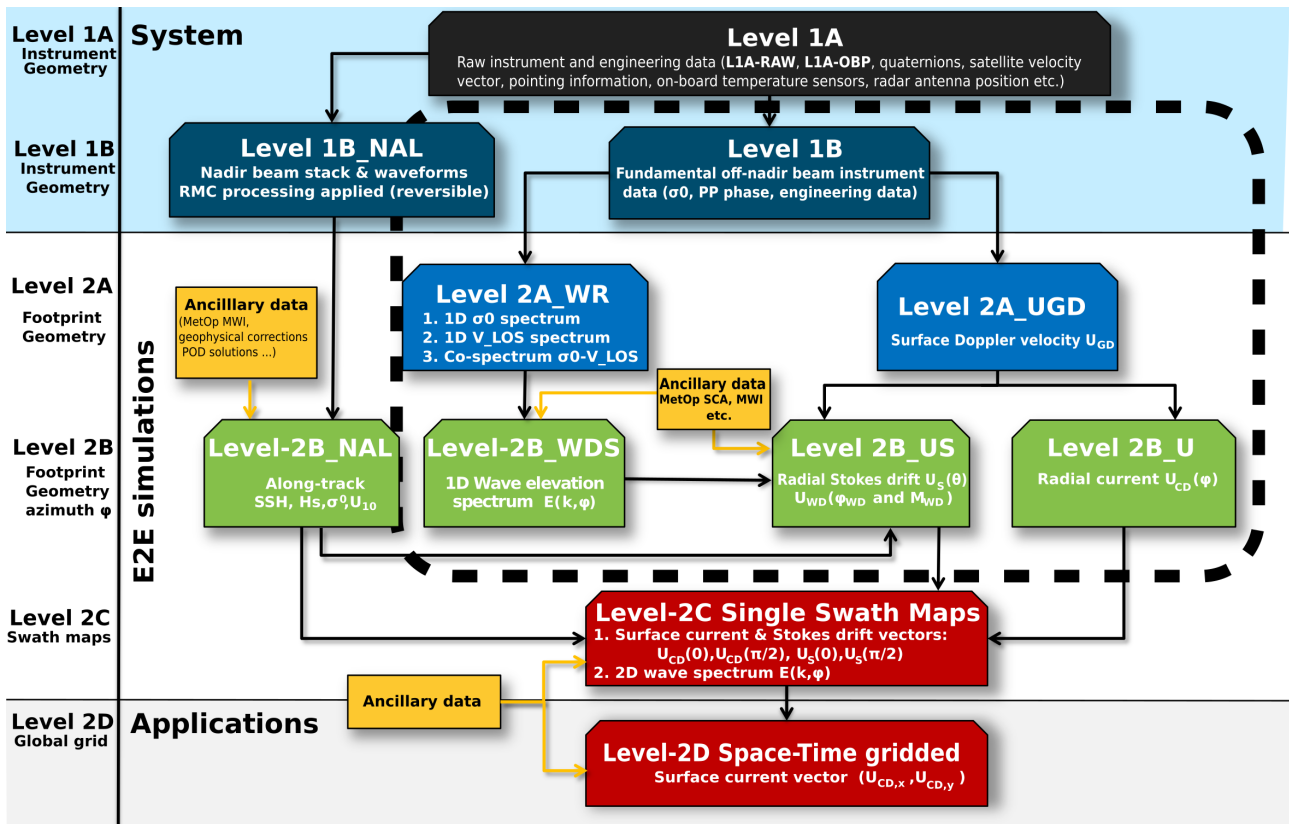
Figure 3: General flow-chart of SKIM products. The part in the dashed box is more detailed in Figure 5.

1.3 Overall flow chart

The sequence of products and algorithms described in the present document is summarized in the general flow-chart (Fig. 3). All notations are detailed below.

For some algorithms, spatial "boxes" will be defined for the first step of the splitting of U_{GD} into $U_{CD} + U_{WD}$. Here we have chosen boxes of 50 km, starting from a (0,0) box centered on the nadir beam (Figure 4). The box size and location may be adjusted in later versions.
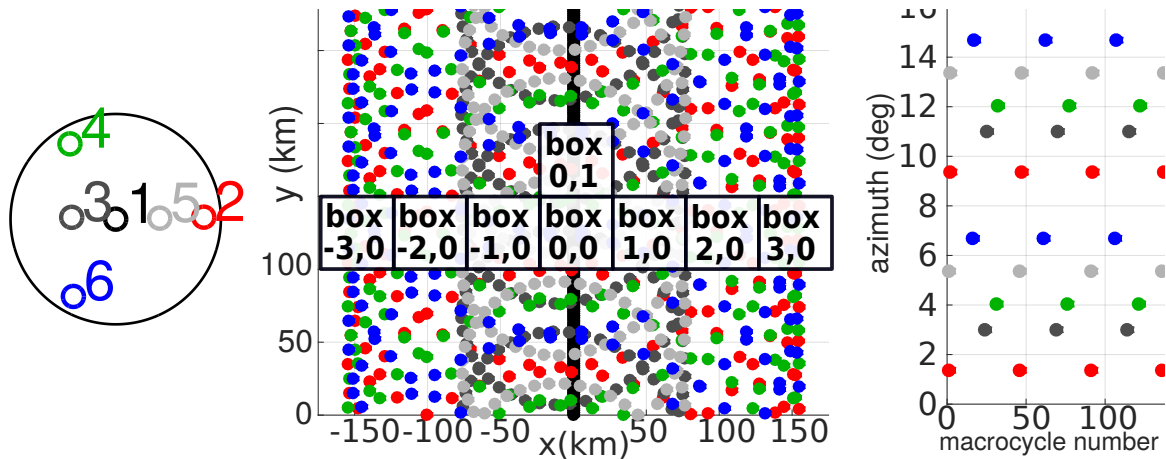

Figure 4: Pattern of beams (left), which rotate anti-clockwise when looking at their footprints on the ground, and their ground footprint (center) used in the present document assuming perfectly periodic patterns along track with a period of 45 macro-cycles, defining a mega-cycle. The actual azimuth diversity (right plot) combining all beams has been fine-tuned by shifting the azimuth of beam 3 by 3.7 degrees on the rotating plate. This is probably not critical for the present analysis.
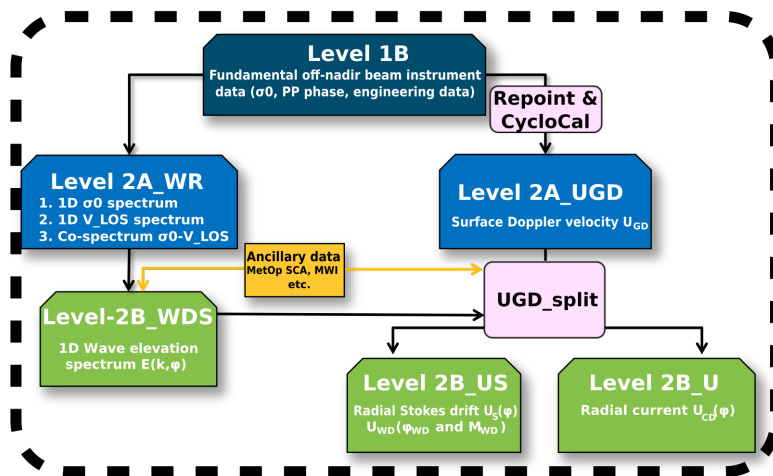
Figure 5: Focus of the present document, in particular the "Repoint" and "UGD_split" algorithms

The present document focuses on the part from Level-1B to Level-2B, as detailed in Figure 5. We particularly describe the "Repoint" algorithm (section 2.5) and the "splitting" of the Geophysical Doppler into waves and current contributions (section 5). Before going into the inversion, it is necessary to explain the forward model and its sensitivity to the sea state, radar parameters and viewing geometry.

2 Non-geophysical Doppler

2.1 Geometrical effect in non-geophysical Doppler: true pointing, true mispointing and apparent mispointing

We first have to describe the geometry of the measurement. In practice, measuring a 1 cm/s velocity from a spacecraft flying at 7 km/s requires a very accurate knowledge of the geometry: the azimuth angle must be known within 1.4 microradians, while the elevation angle accuracy is even more strict, by a factor $\tan(\theta)$, which translates to an accuracy requirement for altitude with respect to the sea surface of the order of 5.4 cm and the same range accuracy, which translates to a timing accuracy of 0.18 ns.

For the system definition, difference reference frame must be taken into account, properly representing the conical scanning of the horn plate and the resulting motion of the radar beam, as depicted in figure 6.
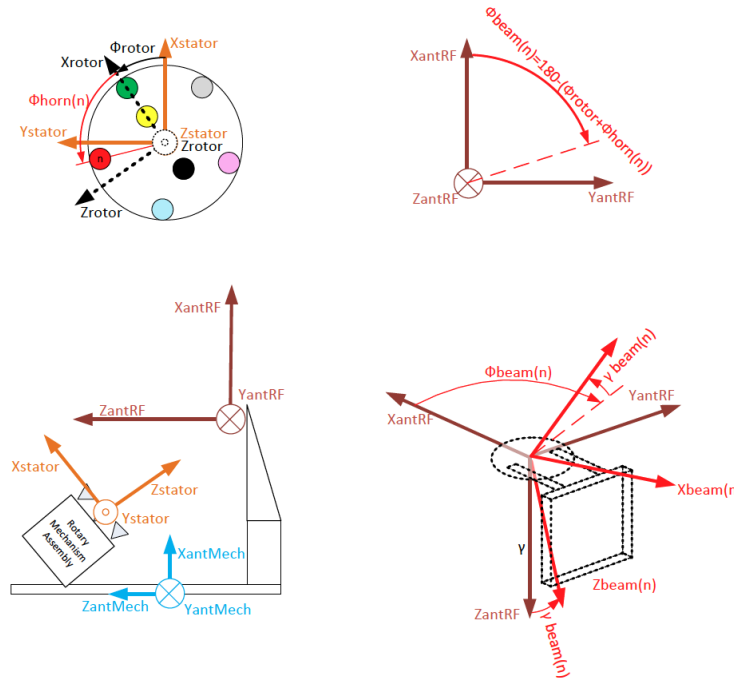

Figure 6: Frames of reference associated to the spacecraft and antenna (Courtesy E. de Witte, ESA)

Our interest is the motion of the ocean relative to the solid Earth. We thus define the 3-component velocity vector of the platform, relative to the local Earth velocity (at the location of the measurement footprint),

$$\mathbf{V} = \mathbf{V}_p - \mathbf{V}_E = (V_x, V_y, V_z). \tag{8}$$

For practical purposes, it is convenient to estimate V_{NG} from a knowledge of the 3-component velocity vector of the platform (V_x, V_y, V_z) relative to the local Earth velocity (including Earth rotation), and radar boresight pointing angle in elevation θ_b and azimuth φ_b has a unit vector

$$\mathbf{e}(\theta_b, \varphi_b) = (\sin\theta_b \sin\varphi_b, \sin\theta_b \cos\varphi_b, \cos\theta_b) \tag{9}$$

with $\varphi = 0$ corresponding here to the along-y axis direction, and the directions are counted clockwise, following the convention of Rodríguez et al. (2018). The angles are the angles *to* which the radar is pointing, which correspond to the
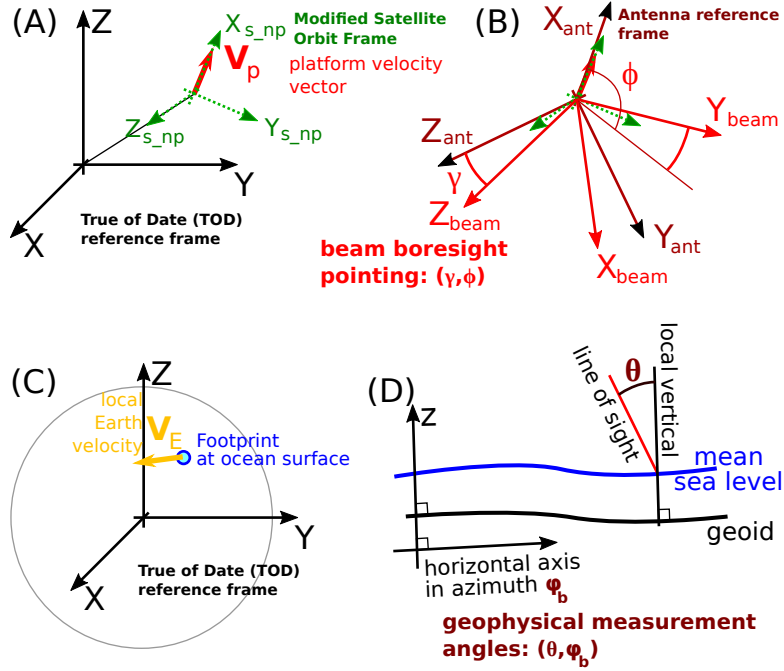
Figure 7: Frames of reference associated the Earth and the geophysical measurement

angle *from* which the echo is coming. Note that φ_b and θ_b are transformed from the antenna boresight pointing angles ϕ and γ, determined in the antenna reference frame (see Fig. 7), by the proper chain of rotations (to be detailed later).

Working in the local frame of reference, pictured in Fig. 7.D, we take the scalar product of the relative platform velocity vector and the pointing vector, giving a line of sight geometric velocity

$$V_{\text{geo}}(\theta_b, \varphi_b) = (V_x \sin \varphi_b + V_y \cos \varphi_b) \sin \gamma_b + V_z \cos \gamma_b = V_h \cos(\varphi_b - \varphi_t) \sin \gamma_b + V_z \cos \gamma_b, \tag{10}$$

where V_h is the horizontal platform-Earth relative velocity, φ_t is the direction of that vector velocity corresponding to the ground track orientation. In this calculation the geometry uses a figure of the Earth based on the actual sea surface topography (including the geoid, tides and atmospheric loading). See section 2.5 and Rodríguez et al. (2018) for a discussion of topography effects.

The knowledge of pointing is very sensitive given the large velocity of the platform, especially the azimuth that is largely controlled by the yaw of the aircraft and the antenna pattern. From an aircraft flying at 120 m/s, a mispoiting of $1°$ in azimuth produces an error on the geophysical Doppler U_{GD} up to 2 m/s. From a satellite flying at 7 km/s, a 1 cm/s accuracy requires a pointing knowledge of 1.4 microradians. Fortunately, thanks to the conical scanning of the SKIM antenna and the measurements of different beams with neigboring footprints, the the time-varying pointing misknowledge produces a spatial pattern of line of sight velocity that is very specific and can be separated from the geophysical signal. This is the basis of the Cyclo-calibration (see other technical note by Dibarboure, elouis & al.).

2.2   Gradients of NRCS contribution to the non-geophysical Doppler

Besides an error in the knowledge pointing error, an apparent skew-pointing of the radar beam can be caused by a non-homogeneous distribution, within the observed ocean scene, of the normalized radar cross section (NRCS) $\sigma^0(x, y, \theta, \varphi)$.
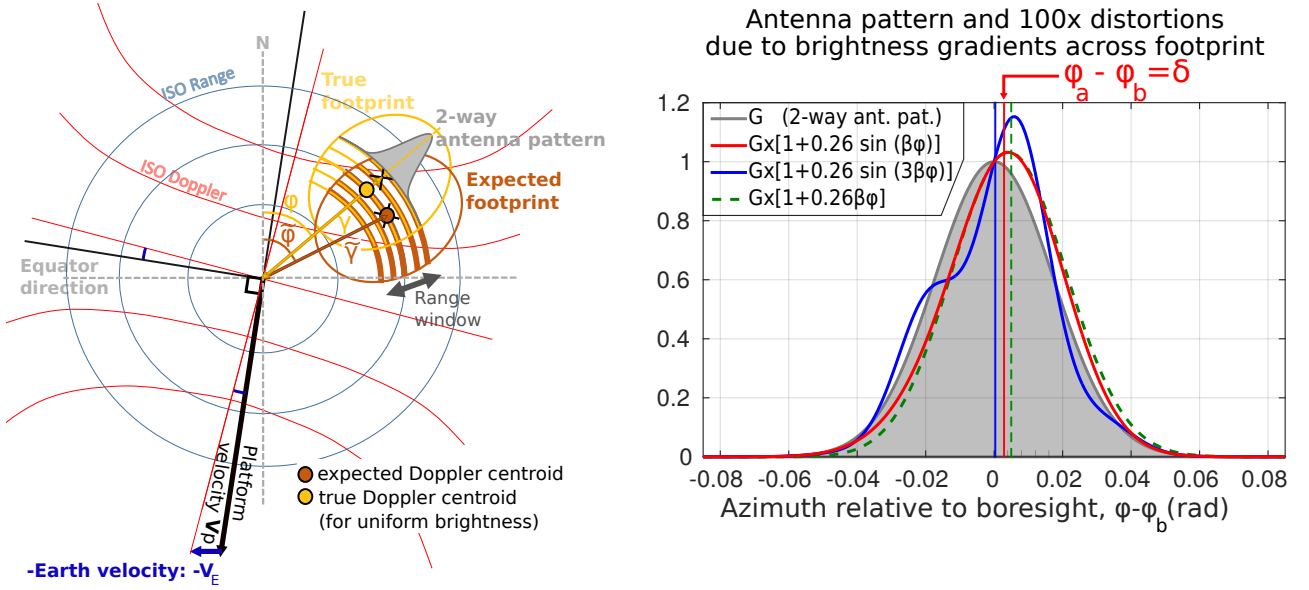
Figure 8: Left: True pointing. The attitude drift changes the antenna footprint direction and shifts the Doppler centroid. Here (γ, φ) are the expected coordinate of the antenna gain ground projection while $(\tilde{\gamma}, \tilde{\varphi})$ are the shifted version of these coordinates by the attitude mis-knowledge, adapted from Delouis et al.. Right: apparent pointing φ_a. Examples of 2-way antenna gain G as a function of azimuth and distortions (exaggerated 100 times) induced by σ^0 gradients on the power integrated by the radar in the azimuth direction across the antenna pattern (grey curve). Three examples of asymetric distortions are given: a sine function with $\beta = \sin\theta/\alpha$, a 3-times faster varying sine function, and a linear trend. If the azimuth φ correlates with the geometrical Doppler, then the distortion produces an apparent velocity error V_δ which corresponds to an apparent mispointing indicated by the vertical lines.

This NRCS is a property of the ocean surface that varies as a function of the horizontal position (x, y) due to the presence of waves, varying winds, currents, surfactants, sea ice and all the physical properties of the sea surface. The NRCS also varies with the viewing geometry, and some azimuth changes can be large enough to have a large impact on the Doppler. Both effects give apparent mispointings in elevation ε and azimuth δ. The full non-geophysical Doppler can be expressed as

$$V_{NG} = V_{\text{geo}}(\theta + \varepsilon, \varphi_b + \delta), \tag{11}$$

that can also be written as an additional velocity component,

$$V_{NG} = V_{\text{geo}}(\theta, \varphi_b) + V_\delta. \tag{12}$$

For the particular case of weak and large scale variation of σ^0 with φ, assuming a simple Gaussian 2-way radar antenna pattern of half-width α in azimuth, an analytical expression can be obtained for the apparent mispointing, as detailed in Appendix A, see also Rodríguez et al. (2018) and Marié et al. (2019),

$$\delta = \frac{\alpha^2}{\sin^2\theta} \frac{1}{\sigma^0} \frac{\partial\sigma^0}{\partial\varphi}. \tag{13}$$

Using a 1-way antenna pattern width $\theta_{3dB}^2 = 8\log(2)\alpha^2$, for SKIM $\alpha \simeq 0.0042$ rad (0.24 degree, which is defined from the $\theta_{3dB} = 0.57°$ for $\theta = 12°$, and $\theta_{3dB} = 0.60°$ for $\theta = 6°$), and at $\theta = 12°$, the change of azimuth between the center of the (2-way) footprint and the edge of the footprint is $\alpha/\sin\theta = 1.1°$.

Our eq. (13) corresponds to a line-of-sight velocity change

$$V_\delta = \frac{\theta_{3dB}^2/4}{8\sin\theta}\frac{1}{\sigma^0}\frac{\partial\sigma^0}{\partial\varphi}(V_x\cos\varphi - V_y\sin\varphi).$$ (14)

which is consistent with the dominant term in the more detailed analysis by P. Dubois (personal communication, see upcoming report on the SKIM End to End Performance Simulator).

2.3 Azimuthal gradients of NRCS

For a uniform wind the azimuthal variation of σ^0 at near-nadir incidence comes from the difference between cross-wind and down-wind mean square slopes (Cox and Munk, 1954; Munk, 2008), an effect that should be relatively weak for wind speeds of 5 m/s or less. For a wind speed of 7 m/s and fully developed sea state $\partial\sigma^0/\partial\varphi/\sigma^0$ is of the order of 0.5 for $\theta = 12°$. This gives an apparent mispointings of the order of 25×10^{-6} rad, which would correspond to a 18 cm/s error on V_{NG} projecting to a 90 cm/s error on U_{GD}.

A typical azimuthal variation of σ^0 is given by

$$\sigma^0 \simeq a_0 + a_1\cos(\varphi - \varphi_w) + a_2\cos[2(\varphi - \varphi_w)]$$ (15)

with φ_w the wind direction. For near-nadir angles, the coefficients a_0, a_1, a_2 are functions of the incidence angle θ and the surface slope statistics. In a first approximation, the slopes can be considered Gaussian, and completely determined by the mean square slopes in direction x and y and the cross term mss_{xy}.
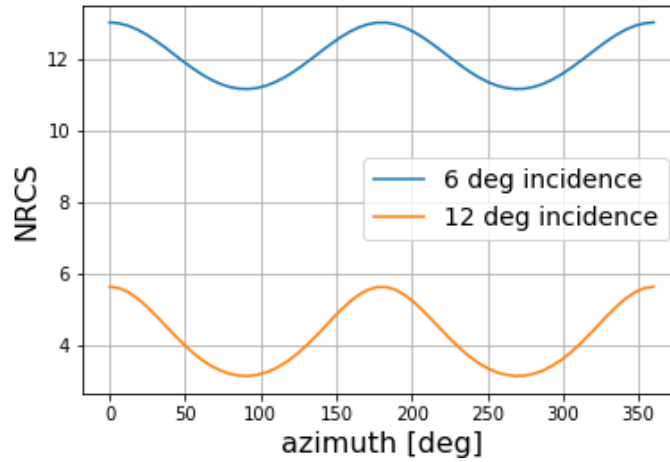
Figure 9: NRCS azimuthal variations for a fully developed wave spectrum given by Elfouhaily et al. (1997) for a wind speed of 7 m/s in direction $\varphi = 0$.

For a spectrum symmetric about the x-axis mss_{xy} is zero so that it is common to use the wind direction as the x-axis and use the down-wind and cross wind mean square slopes (Cox and Munk, 1954; Munk, 2008). In general, the principal axis of the mean square slope ellipse is not exactly in the wind direction.

For a fully developed wind-sea with 7 m/s, the parametric spectrum shape by Elfouhaily et al. (1997) gives $a_0 \simeq 4.5$ dB, $a_1 = 0$ and $a_2 \simeq 1.2$ dB for $\theta = 12°$ as illustrated in Fig. 9. For this symmetric variation of σ^0, with the same value between

Figure 10: Example of the contributions to the line of sight velocity V_{LOS} for a fully developed wind sea for 7 m/s with a spectrum specifi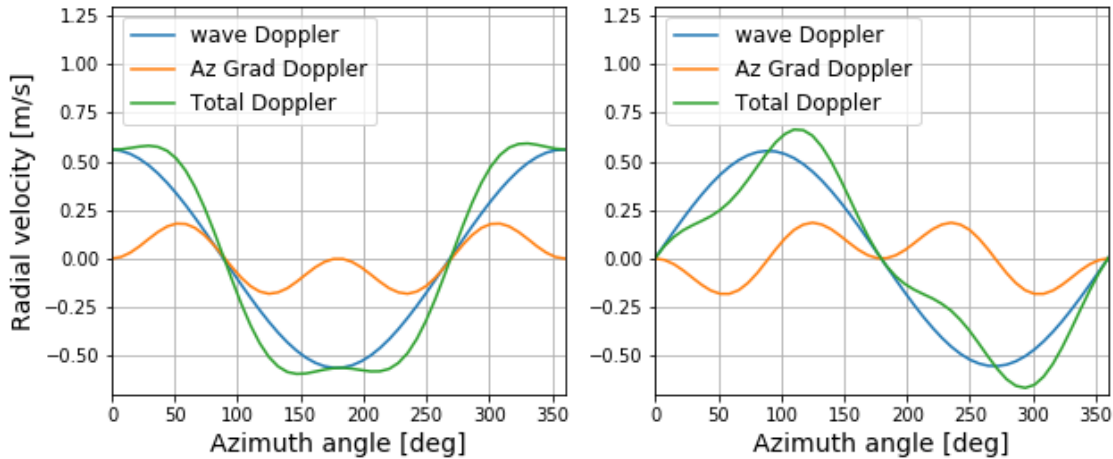ed by Elfouhaily et al. (1997). The "Az Grad Doppler" is V_δ as given by eq. (14). Left is for a wind direction opposite to the platform-Earth relative velocity vector **V**, and right is for a wind direction perpendicular to **V**, both for $\theta = 12°$. The wave Doppler contribution is added for magnitude comparison. All velocities must be multiplied by $1/\sin\theta \simeq 5$ when converted to surface current in U_{GD}.

downwind, here $\varphi = 0$ and upwind, here $\varphi = 180°$, the apparent velocity associated to the azimuthal gradient of the NRCS is completely determined by the ratio a_2/a_0.

For the same $\partial\sigma^0/\partial\varphi/\sigma^0$ gradient, the apparent mispointing given by eq. (13) increases by a factor 4 for the 6° beams because the footprints have roughly the same size (3 km radius for the 2-way 3-dB pattern) but are located closer to the nadir, and thus are seen with a larger azimuthal diversity. This is partly compensated by the reduction in the σ^0 variation.

The example modulation shown in Fig. 9 has a upwind-crosswind variation of 2.4 dB at $\theta = 12°$, and 2 dB at $\theta = 6°$. This magnitude is twice what is found in SWIM data in Ku-band at much higher winds, as shown on figure 11 and it is generally lowest around 7 m/s. This is also confirmed by GPM data in Ka-band and Ku-band shown in Fig. 12. Observations include an upwind / downwind asymmetry that is not included with the description of the sea state based on Elfouhaily (1997), but is due to the asymmetry of waves (e.g. Cox and Munk, 1954; Walsh et al., 2008).

We thus expect that the Elfouhaily-based simulations overestimate the values of $\partial\sigma^0/\partial\varphi/\sigma^0$ by a factor around 2, and that the real azimuthal variation has some upwind/downwind asymmetry that is not represented in the simulations. In practice we expect to use a GMF using downwind, updwind and cross wind σ^0. We also note that the downwind/crosswind ratio is related to the downwind/crosswind mean square slopes (Cox and Munk, 1954; Bréon and Henriot, 2006).
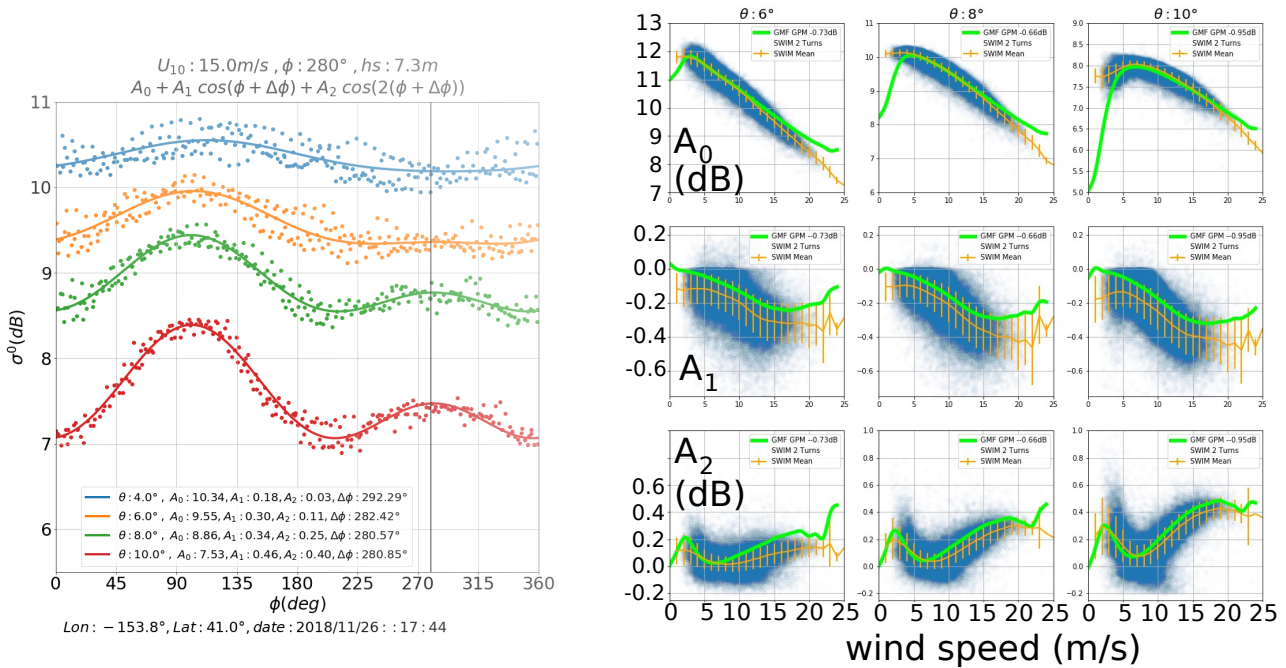
Figure 11: Left: Example distribution of of σ^0 in Ku-band as measured by SWIM, for a high wind and wave case. Right: distribution of modulation factors A_1 and A_2 for the month of January 2019. SWIM analysis by V. Gressani et al.
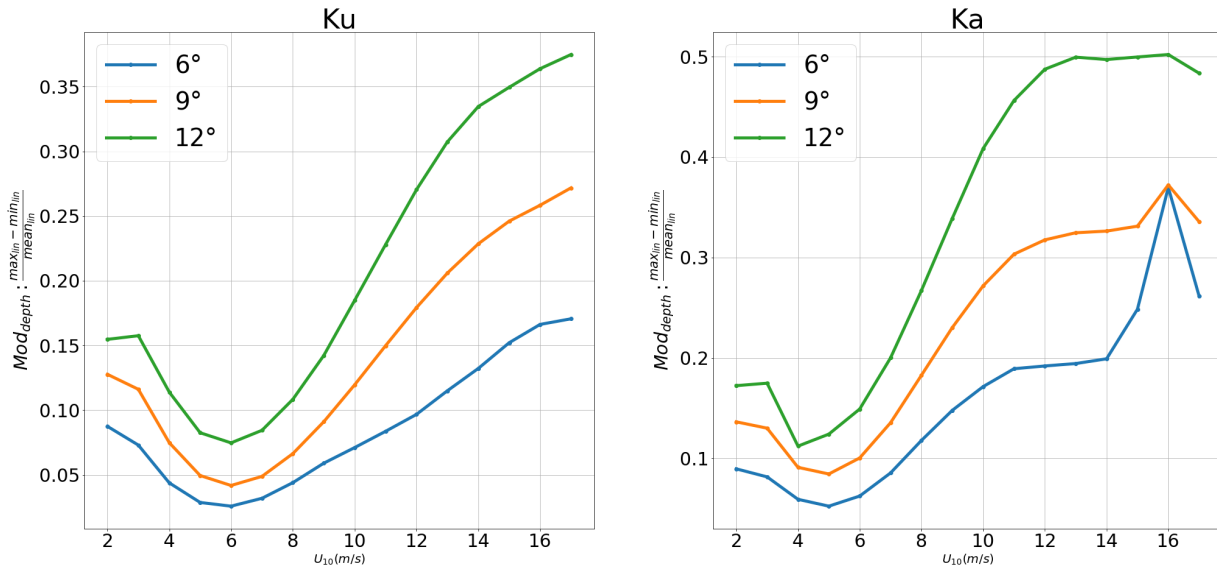

Figure 12: Climatological modulations factor $(2A_2)/A_0$ estimated from GPM data. Analysis by V. Gressani et al.

2.4 Spatial gradients of NRCS

The radar integrates the echoes in a given range gate over which the surface normalized radar cross section σ^0 is not constant. As a result, the Doppler centroid is shifted in a way similar to the effect of a mispointing. Further, the shape of the Doppler spectrum is distorted by the patterns of σ^0 instead of being simply given by the antenna pattern. This distortion is usually corrected by considering a "look power balancing" correction (Madsen, 1989; Hansen et al., 2011). But let us first estimate its magnitude.

When σ^0 varies at scales comparable to the footprint, e.g. $\sigma^0 = a_0[1 + \varepsilon \sin(\beta \varphi)]$, then

$$\delta = \frac{\varepsilon \alpha^2 \beta}{\sin^2 \theta} \exp(-\beta^2 \alpha^2 / 2 \sin^2 \theta). \tag{16}$$

For a fixed amplitude ε, this mispointing is maximum for $\beta = \sin \theta / \alpha$, where we recall that $\alpha / \sin \theta$ is the standard deviation of the Gaussian antenna pattern when projected on the ground. For smaller scales, with higher values of β, the fluctuations of σ^0 average out, while the larger scales only give a small variation across the antenna pattern. For large scale variations, $\beta \to 0$ and $\varepsilon \beta \to \partial \sigma^0 / \partial \varphi / \sigma$, so that we recover eq. (13).

A first order of magnitude of the apparent mispointing associated with a crest-to-trough change of σ^0 of 0.1 dB (i.e. $\varepsilon = 0.012$) varying like $\sigma^0 = a_0[1 + \varepsilon \sin(\varphi \sin \theta / \alpha)]$ is $\delta = 120 \times 10^{-6}$ rad, corresponding to a bias up to 90 cm/s. For the harmonics $\beta = n \sin \theta / \alpha$, the apparent mispointing is only to 44% of that value for $n = 2$ and is as low as 5% for $n = 3$, and 0.2% for $n = 4$. Namely it is the large scale oscillations across the footprint that really matter.

Since we are having fun with horror stories, an even scarier number is obtained by considering that the σ^0 variation takes the shape of a sharp front in the form of a Heaviside function,

$$\sigma_0 = 1 + 0.5 \varepsilon \varphi / |\varphi| \tag{17}$$

then the mispointing is

$$\delta = \frac{\varepsilon \alpha}{\sin \theta \sqrt{2\pi}}. \tag{18}$$

In this case, for $\varepsilon = 0.0593$ corresponding to a 0.5 dB jump we find $\delta = 1000 \times 10^{-6}$ rad, i.e. a maximum error of 7.2 m/s on the retrieved current.

So what will happen? Is SKIM dead? No. Large Doppler shifts shall certainly occur. But, fortunately, the ocean is – most of the time – the most homogeneous surface you may imagine. For instance, a very large surface current gradient, i.e. 0.5 m/s over 100 m Rascle et al. (2017), leading to measurable localized roughness changes, only gives a relative NRCS change under 10 % (less than 0.4 dB) for moderate wind conditions, and this is a symmetric spike over a 50 m wide region, that will average to 0.02 dB over 1 km. Largest NRCS changes will thus mostly occur under for wind speeds less than 2 m/s.

A quantitive estimation of the occurence of σ_0 gradients at the scales of interest can combine combine a wide range of data. Ideally this could be made from SAR imagery in Ka-band, or optical imagery (Kudryavtsev et al., 2017) from which the surface slope statistics can be estimated and converted into Ka-band σ^0 gradients after performing the proper average along a SKIM iso-Doppler line. Here we use the imaging characteristics of the SWIM instrument on CFOSAT for which 6 months of data is already available.

2.4.1 Lower bound from SWIM modulation spectra

The data acquired by the SWIM Ku-band radar (Hauser et al., 2017) offers an interesting measurement geometry by providing integrated σ^0 values over narrow strips with $dx \simeq 6$ m and $L_y \simeq 13$ km (this is the 2-way antenna pattern width). Although the NRCS fluctuates by about 1 dB over a few range gates, this is essentially associated to ocean waves. We also
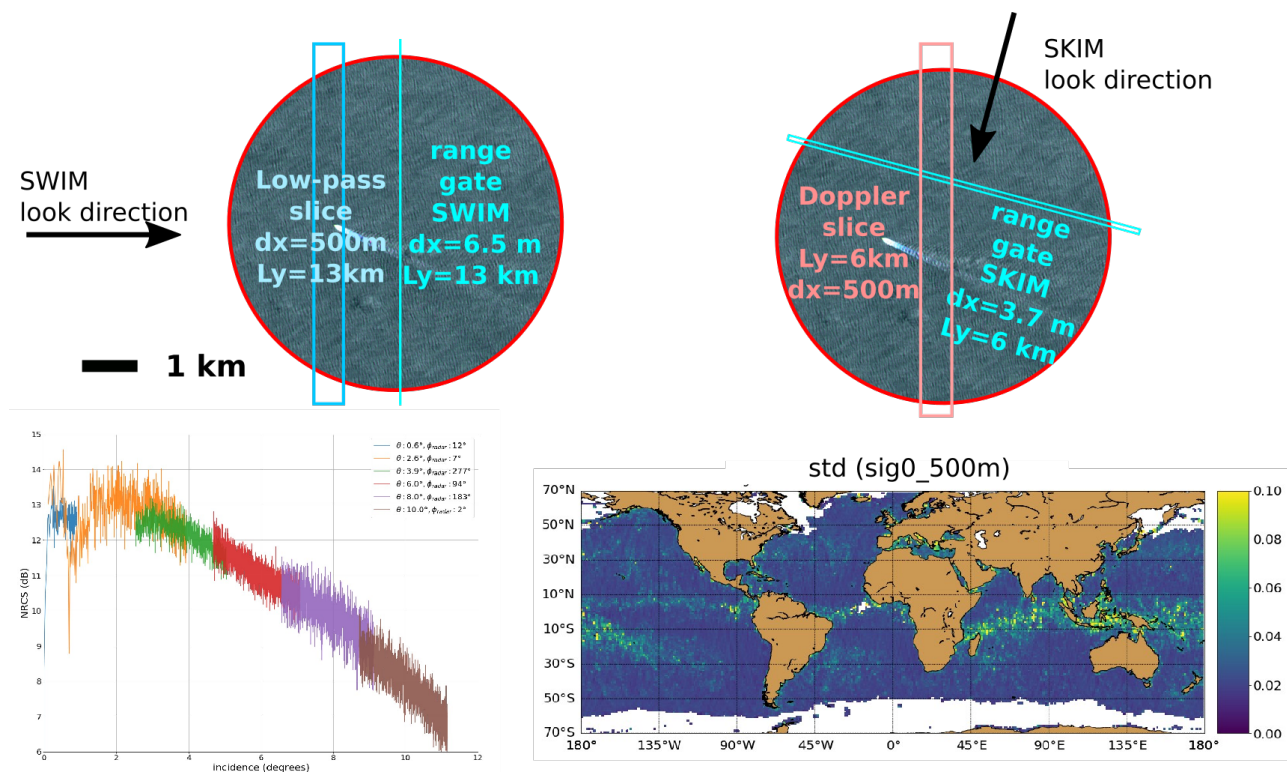
Figure 13: Averaging geometry of SWIM, and relevant averaging on SKIM for looking at unresolved variability of σ^0 in azimuth. Bottom left: example of σ^0 as a function of the incidence angle with the different colors corresponding to different beams, Bottom right: global map of $std_{500\ m}(\sigma^0)$ for January 2019. SWIM analysis by V. Gressani et al.

note that the imaging of small scales are impacted by migration and processing, but this is not the case for the $L_x > 500$ m scales that we consider here.

In particular a rain flag has been proposed by Gressani et al. based on the standard deviation of σ^0 after filtering with a Gaussian filter with $\sigma = 500$ m, corresponding to a 1 km averaging scale (More exactly the power spectrum is reduced by half at a wavenumber $k = 0.002\sqrt{\log(2)}$ rad/m, i.e. for wavelengths larger than 3.8 km). Accounting for the larger integration in SWIM compared to SKIM, we may estimate that the standard deviation of σ^0 over a 500 m by 6 km SKIM Doppler slice is of the order of $\sqrt{2}$ times what was found for SWIM, i.e. 0.03 dB, which should translate to almost the same value for Ka-band at $12°$ incidence (Nouguier et al., 2016). Instead of 500 m, the same analysis was repeated for 250 m, 1 km, 2 km, giving similar results.

The azimuthal wavenumber for which the apparent mispointing is largest was found to be $\beta = \sin\theta/\alpha$, which corresponds to a wavelength of 17 km. We assume here a constant spectral density in the range of wavelength between 3 and 20 km, consistent with previous analysis of average wind speed regimes (Young et al., 2000), caused by the fluctuations of winds, currents, temperature etc. and resulting in random Gaussian fluctuation. The analysis by Gressani et al. tells us that the typical variance between 3.8 and 20 km wavelength (i.e. a spectral bandwidth of $\Delta_k = 0.0013$ rad/m) is 0.03^2 dB^2. As a result, a random distribution if σ^0 gives a uniform spectrum with the same variance for all n of a modulation of the form

$$\sigma_0 = \overline{\sigma}_0 \left[1 + b_n \sin(n\varphi \sin\theta/\alpha)\right] \tag{19}$$

Performing a discrete Fourier transform on a 17 km window, with a spectral resolution $dk = 2\pi/(17\ \text{km})$ gives us a 17 km sine component with a mean variance of $0.03^2 dk/(2\Delta_k)$ in dB^2. Hence a 0.03 dB standard deviation gives a mean values

PDFs of std(sig0_500 m)

Figure 14: Distribution of the standard deviation of 500 m low-pass filtered SWIM data for January 2019. SWIM analysis by V. Gressani et al.

of the Fourier components $b_n = 0.03 * \sqrt{dk/(2\Delta_k)} = 0.011$ dB, corresponding to $b_n = 0.0026$ in linear units. As a result, the typical mispointing for the most effective Fourier component is 27×10^{-6} rad, with a maximum velocity error of 20 cm/s. A random sum of all Fourier components, with positive and negative contributions, will typically give less.

As shown in figure 13, the errors can be 5 times as large, but they are generally associated with rain. We may use a threshold at 0.1 dB on the SWIM data which translates to a 40 cm/s random error on the U_{GD} estimate for 12° incidence. This only excludes 2% of the data which are generally rain cases. Using a lower a lower threshold excludes more data.

We also note that σ^0 in Ka-band is 3 to 20 times more sensitive to temperature gradients than Ku-band (Meissner and Wentz, 2016; Vandemark et al., 2016). Typically a 1 K variation around 20°C produces a 0.01 dB change in σ^0 for Ka-band. This effect should thus be further investigated as it will amplify a little the variations of σ^0 that we have just discussed.

2.4.2 Upper bound from large scale σ^0 variations

The estimate of typical σ^0 variations given by SWIM in Ku-band is confirmed by further analysis of SARAL-AltiKa data, which as the benefit to also include stronger atmospheric effects that are relevant for SKIM. An analysis was performed by F. Boy using his adaptive retracking algorithm that provides a much less noisy estimate of the 40 Hz σ^0 that the GDR data, followed by filtering very high resoluton noise, and editing for rain and so-called σ^0 blooms. Figure 15 shows values (one dot for every 40 Hz data) over two cycles, of $d\sigma^0/dx$ with σ^0 computed with $dx = 0.175 * 34$ km, by taking the difference between the data at $i+17$ and $i-17$ where i is the local index.
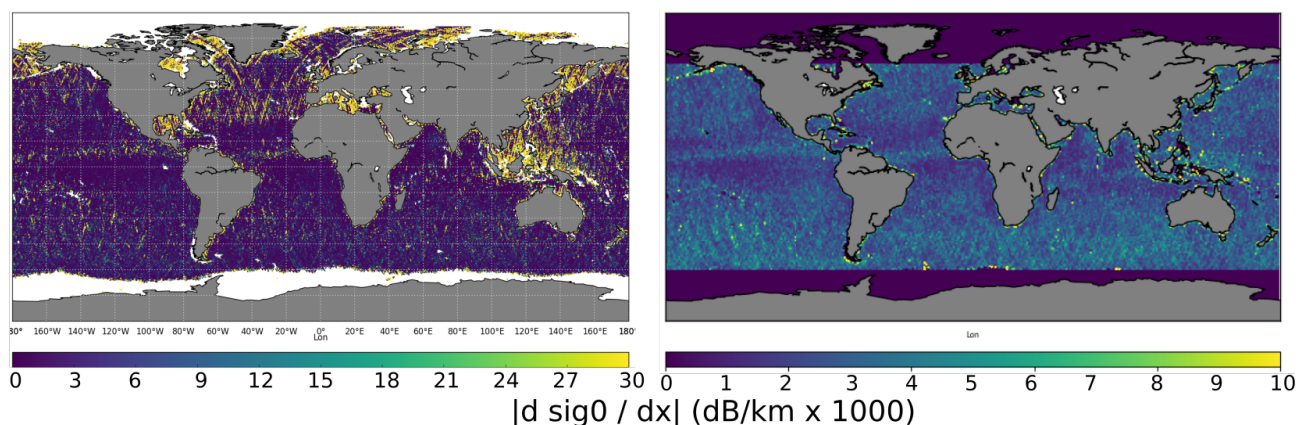

Figure 15: Map of σ^0 gradient in dB per km, Courtesy F. Boy (CNES) .
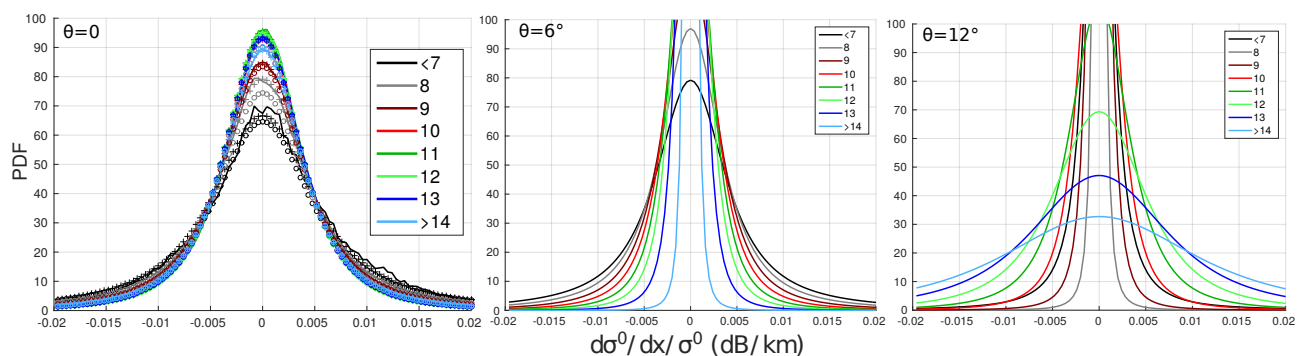
Figure 16: Left: PDF of σ^0 gradient in dB per km at nadir, Courtesy F. Boy (CNES). Fitting a Student-type distribution, the nadir PDF was transformed to $6°$ and $12°$ assuming a simple variation of σ^0 with incidence angle . The Student fit is shown by the '+' symbols, and the 'o' is the Student distribution with a width σ_X and v degrees of freedom, parameterized as a function of σ_0^0.

For any given value of σ^0, this data is consistent with a Student-type distribution, with the gradient X in dB, and σ_0^0 in dB,

$$\text{PDF}(X) \simeq 10^{\left\{a - (3+v)\log\left[1 + X^2/\left((1+v)\sigma_X^2\right)\right]\right\}/10} \tag{20}$$

$$v = 4.635\exp(-0.03(\sigma_0^0 - 12)^2) \tag{21}$$

$$\sigma_X^2 = 0.0067^2 \times 10^{-(\sigma^0+1.5)^2/100} + 4.9 \times 10^{-7}\sigma_0^0, \tag{22}$$

where a is adjusted to give a unit integral of the PDF.

Most of the ocean has average nadir gradients under 0.003 dB/km. Assuming that these gradients are only due to ocean surface properties (i.e. excluding a residual retracker noise and atmospheric effects), they can be converted to other incidence angles using the Gaussian sea state approximation

$$\sigma^0 \simeq= \frac{R^2}{\text{mss}_{\text{Ka}}\cos^4\theta}\exp(-\tan^2\theta/\text{mss}_{\text{Ka}}) \tag{23}$$

with $R \simeq 0.55$ (Vandemark et al., 2016). With this assumption, the PDF of the gradient at any incidence angle is obtained by stretching X in the analytic expression (20).

Converting these numbers to an azimuthal gradient for SKIM requires to take into account the averaging geometry of AltiKa and the different viewing geometry of SKIM. It should be checked if the gradient for a given value of σ^0 varies with H_s. Indeed, following Chelton et al. (1989) we expect the "oceanic footprint area" of AltiKa varies with H_s

$$A_A = \pi H(c\tau + 2H_s)/(1 + H/R_E), \tag{24}$$

where R_E is the Earth radius and τ is the effective pulse length after range compression, for AltiKa, $c\tau \simeq 0.64$ m. For this we have used a average H_s for each value of the nadir σ^0 that is consistent with Lillibridge et al. (2014),

$$H_s \simeq 1.5 + 5/(\sigma^0 - 6)^2 \text{ m}. \tag{25}$$

A more detailed analysis of AltiKa data should be done separating the effect of H_s and σ^0.

If we assume the corresponding averaging area for SKIM is A_S, taken to be half the footprint area, then the effective gradient is reduced by a factor $\sqrt{A_A/A_S}$,

$$\frac{\partial\sigma_\theta^0}{\partial\varphi} \simeq H\sin\theta \left.\frac{\partial\sigma_0^0}{\partial x}\right|_{\text{altiKa}} \frac{\partial\sigma_\theta^0}{\partial\text{mss}}\frac{\partial\text{mss}}{\partial\sigma_0^0}\sqrt{\frac{A_A}{A_S}}. \tag{26}$$

This gives an average mispointing varying from 4 to 30 microradians at $12°$ with the higher values given by the lower wind speeds. The trend is opposite for $6°$ with higher values at average winds ($\sigma^0 = 10$ dB), and low errors at low winds.
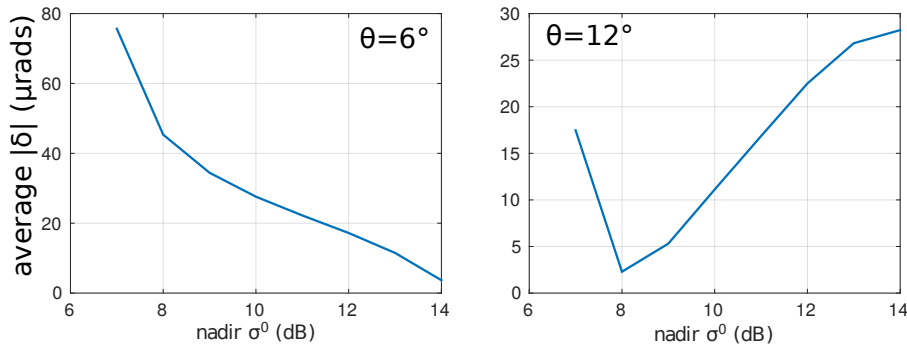
Figure 17: Average value of the magnitude of the mispointing using the σ^0 gradients PDF shown in Fig. 16, and eq. (26). The very large sensitivity with incidence angle may make it possible to use the difference in Doppler between the first half and last half of the range windows as an additional flag.

These numbers are broadly consistent with the effect of a the typical 0.01 dB sine component amplitude across the footprint as discussed from SWIM data in Ku-band at $10°$.

This analysis relies on the assumption that the analysed AltiKa σ^0 gradients, after editing for rain and σ^0 blooms, is entirely due to the ocean surface with no residual tracker noise and atmospheric effect. We note that such variations of σ^0 are comparable to the cloud Path Integrated Attenuation in Ka-band (Battaglia et al., submitted, see Figure 18). It is thus possible that the measured gradients of σ^0 on unflagged SARAL-AltiKa have a significant contribution from attenuation effects, that would corrupt our transformation from nadir to other incidence angles. Our estimate is thus probably an upper limit of the true σ^0 gradient at 12 deg. for high winds. We should thus investigate the mispointing over realistic cloud
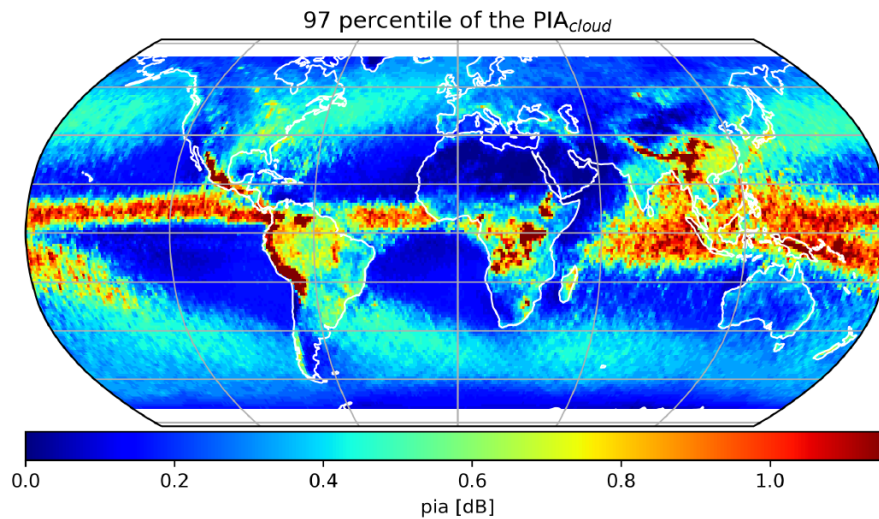

Figure 18: 97th percentile of the two way PIA expressed in dB for clouds, based on GPM Level 2 DPR product, version 05A and Level 2 GMI-GPROF product, version 05A, reproduced from Battaglia et al. (submitted).

scenes. Even if the cloud-associated PIA is 0.5 dB 3% of the time, its variation across a SKIM footprint should be much less.

2.5   Estimation of U_{NG}: combination of pointing and NRCS variations

Pointing effects covered here contain both the geometrical effect associated to platform and instrument microvibration and thermoelastic deformation, as well as effects of the non-homogeneity of the σ^0 across the footprint. That latter effect combines both the variation of σ_0 that would occur in a "spotlight mode" imagining that the azimuth would change while illuminating the same location, and the variation occuring due to spatial gradients. Both effects are combined in the measured σ_0 and cannot be separated in the measured σ_0.

In Envisat and Sentinel 1 Doppler data, such effects are corrected for by using the shape of the Doppler spectrum and corrected using a "look power balancing" method (Hansen et al., 2011). Given the accuracy required here (better than 0.01 dB across the footprint), it is unclear whether this will be sufficient. We have therefore chosen to include an additional random error term in the SKIM error budget assuming a sine amplitude ε with a Gaussian distribution of standard deviation of 0.0026.

The large-scale gradients associated to a change in φ shall be estimated from the data in a way similar to SWIM with an expected accuracy of 0.03 dB (TBC) for $A_1 \pm A_2$. The error on A_1 and A_2 should contain effects of spatial gradients of the directional mss that will have to be investigated further, for example using SWIM data, and it is thus not independant of the error on the spatial gradient of σ^0. The value of σ^0 corrected for the large scale azimuthal gradient

$$\widetilde{\sigma}^0 = A_0 + A_1 \cos(\varphi - \varphi_\sigma) + A_1 \cos[2(\varphi - \varphi_\sigma)] \tag{27}$$

is

$$\sigma'^0 = \sigma^0 - \widetilde{\sigma}^0. \tag{28}$$

We still expect to

- either compute a mispointing residual as done by Rodríguez et al. (2018):eq. A26, after a first correction to take into account A_1 and A_2

$$\delta' = \frac{\int_{-\infty}^{\infty} (\varphi' - \varphi_b) \sigma'^0(\varphi') G(\varphi') \mathrm{d}\varphi'}{\int_{-\infty}^{\infty} \sigma'^0(\varphi') G \mathrm{d}\varphi'}. \tag{29}$$

- and/or use the beam displacement (3 km over 36 ms at 12 deg for 6 rpm) and use the σ^0 difference between the first and second half of the cycle and evaluate δ'

A flagging threshold, possibly following what is done on SWIM (Gressani et al.) must be defined above which any correction is expected to leave a residual velocity error larger than 30 cm/s (TBC). We note that the Doppler resolution is best for cross-track azimuths where the velocity error is largest due to the $V_h \sin(\varphi_b - \varphi_t)$ term in eq. (10). In the along-track direction, the error goes to zero as the DBS accuracy also becomes very bad.

Once we have obtained δ we estimate the non-geophysical Doppler velocity using eq. (11), which gives U_{GD} by applying eq. (1),

$$U_{GD} = V_{\mathrm{LOS}} / \sin\gamma - V_{\mathrm{geo}}(\gamma, \varphi_b + \delta + \delta'). \tag{30}$$

where the elevation angle γ is obtained from the measured range R and a knowledge of the mean sea surface height h at the center of the footprint. This knowledge combines the range measurement of the nadir beam and ancillary knowledge of spatial gradients of geoid and tides.

Meaningful estimates for the accuracy requirements on these ancillary datasets can be obtained in the flat-earth approximation. In this approximation,

$$\gamma \simeq \theta \simeq \arccos(h/R) \tag{31}$$

with h the vertical separation between the instrument and the observation point. In that case, the accuracy δ_h necessary to meet the $\delta U_{GD} \leq 1 \mathrm{cm.s}^{-1}$ requirement can be evaluated as,

$$\delta_h \simeq \mathrm{h} \frac{\delta U_{GD}}{|\mathbf{V}|} \tan^2(\theta). \tag{32}$$

The corresponding numerical values are $\delta_h \simeq 1.3$ cm for the $6°$ observations, and $\delta_h \simeq 5.2$ cm for the $12°$ observations. These orders of magnitudes apply to the *total* vertical separation estimation, *i.e.* including the error contributions of spacecraft positioning and sea surface elevation at the observation point (geoid undulation, absolute dynamic topography, tides, inverted barometer correction, etc.). The nadir altimeter payload (with POD) will provide direct observations of the vertical separation in the uptrack/downtrack directions for which this error is most important due to the $\cos(\varphi_b - \varphi_t)$ term in eq. (10). Given the accuracy of the nadir beam of SKIM and greats improvements in knowledge on the geiod (e.g. Zhang and Sandwell, 2016) and time-varying components of the sea surface, we expect that the knowledge error of γ will not contribute more than very few cm/s to the error on U_{GD}.

It is only after that step that the Cyclo-calibration may be applied to remove some possible systematic residual errors associated to pointing error knowledge.

3　Wave contribution to the geophysical Doppler

For near-nadir high-frequency configuration, specular and quasi-specular scattering mechanism applies. Analytically, a Kirchhoff approximation can model electromagnetic wave interactions with the ocean surface, and Nouguier et al. (2018) simply obtained,

$$U_{\mathrm{WD}} \quad = \quad c f_{GD}/2f/\sin\theta \tag{33}$$

$$= \quad \left[\mathrm{mss}_{rt} \frac{1}{\cos^4\theta\,\sigma^0} \frac{\partial(\cos^4\theta\,\sigma^0)}{\partial(\tan\theta)} + \frac{1}{\tan\theta} \mathrm{mss}_{pt} \frac{\partial\sigma^0}{\partial\varphi} \right] \tag{34}$$

$$\simeq \quad M_{\mathrm{WD}} \cos(\varphi - \varphi_{\mathrm{WD}}), \tag{35}$$

where c is the speed of light and f_{GD} is the geophysical Doppler shift. The last line is an approximation that makes the present discussion more simple but is easily extended to non-cosine and asymmetric distributions of $U_{\mathrm{WD}}(\varphi)$.

In eq. (35), the mean slope velocity vector, **msv**, arises from the two-point elevation correlation taken at very short time. Further considering a very-high radar frequency, the main scattering contribution comes from EM fields interacting at very short distances. The surface elevation differences is then well approximated by the surface slope. Consequently, it is the mean slope velocity that govern the geophysical velocity, with components in the range (look) direction r and in the perpendicular p direction,

$$\mathbf{msv} = (\mathrm{msv}_{rt}, \mathrm{msv}_{pt}). \tag{36}$$

We note that for linear (Gaussian) waves, the msv vector is half of the surface Stokes drift vector,

$$\mathbf{msv} \simeq \frac{1}{2}\mathbf{U}_s. \tag{37}$$

It is this important to understand the variability of both terms, the Stokes drift U_S, and the imaging factor related to $\partial\sigma^0/\partial\tan\theta$.

The Stokes drift is an integral of the wave spectrum usually estimated assuming linear wave theory (Kenyon, 1969). Figure 19 shows its typical variation with wind speed for a open ocean site (station PAPA, North Pacific), and a coastal site (Pierres Noires). For any given wind speed, the variability is explained by the sea state. For example, in coastal areas exposed to ocean swell, an offshore low wind will produce a wind sea with a Stokes drift that can be completely canceled by the swell, this is why the 62069 buoy has some very low values of U_s up to 5 m/s, these are not found in open ocean like at station PAPA. In general, U_S is highly correlated with the wind, and the residual is strongly dominated by the significant wave height as shown in Fig. 20 (see also Ardhuin et al., 2009). For version 2 of this note: it would be nice to also show and discuss the difference in angle between Stokes drift and wind direction.

Besides the importance of U_S, the velocity U_{WD} results from the correlation between local orbital motions and variations of the NRCS σ^0. As suggested, this overall correlation is controlled by the imaging capability. Accordingly, the overall radar intensity contrasts and Doppler shifts are linked. For near nadir high-frequency radar measurements, the strength of the modulations are comparable to optical measurements (see Fig. 1 and 2 in Kudryavtsev et al. (2017)), largely governed by the factor $1/\mathrm{mss}_{\mathrm{shape}}$ where $\mathrm{mss}_{\mathrm{shape}}$ relates to a Gaussian-approximation for the quasi-specular fall-off Walsh et al. (1998). This apparent mean square slope is smaller than the total mean square slope Nouguier et al. (2016), possibly accounting for non-linearities and other effects, see for example Chapron et al. (2000); Walsh et al. (2008). In Ka-band this $\mathrm{mss}_{\mathrm{shape}}$ shall thus become very close to the total mss and, to first order, we can approximate $U_{\mathrm{WD}} \simeq U_S/\mathrm{mss}$. It is thus possible to get good order of magnitudes of M_{WD} from the knowledge of the variation of σ^0 with the incidence angle. As illustrated by figure 21, the value of σ^0 is not uniquely determined by the wind speed, and varies significantly with the sea state (Nouguier et al., 2016).

In figure 22 the regime change around $U_{10} = 4$ m/s for $\theta = 6°$, and around 6 m/s for $\theta = 9°$, These conditions correspond to $\mathrm{mss}_{\mathrm{shape}} = \tan(\theta)$. This gives a ratio $G = M_{\mathrm{WD}}/U_s$ of the order of $1/\tan^2(\theta)$. Extrapolating to 12°, the regime change should be around 8 m/s, i.e. close to the most common wind speed, for which $G \simeq 22$.
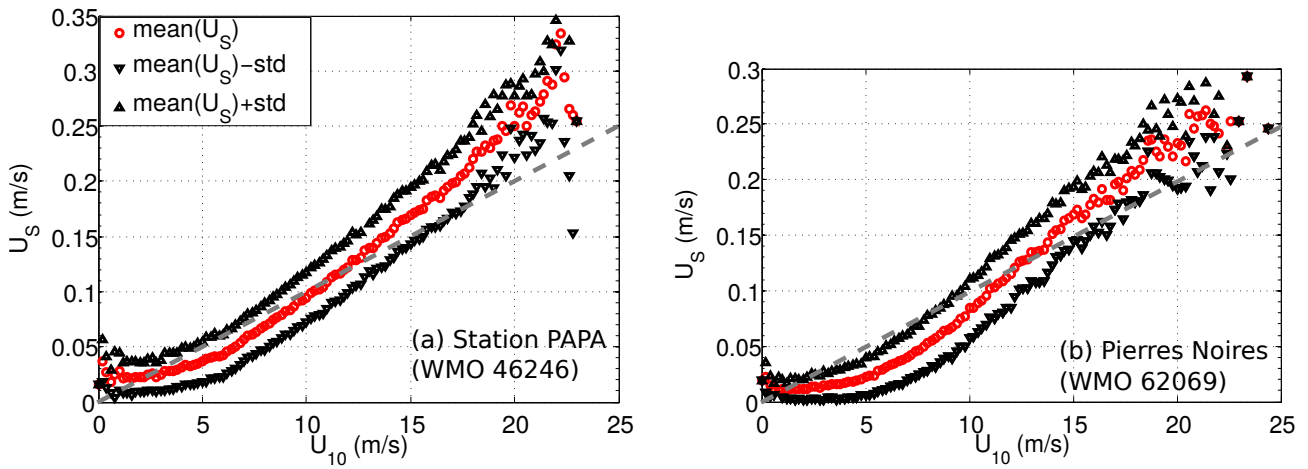
Figure 19: Figure 4. Example of mean value (in red) of the Stokes drift vector norm $U_S = |(U_S(0), U_S(\pi/2))|$ as a function of wind speed for two locations: station PAPA in the northeast Pacific, and buoy 62069 off the French Atlantic coast. The black symbols show the mean ± 1 standard deviation for each wind speed. The dashed grey line is $U_S = 0.01 \times U_{10}$. This estimation covers only frequencies up to 0.58 Hz. Reproduced from Ardhuin et al. (2018). The PAPA station wave data was provided by CDIP and Pierre Noires data from CEREMA, in both cases the wind comes from ECMWF operational analyses.
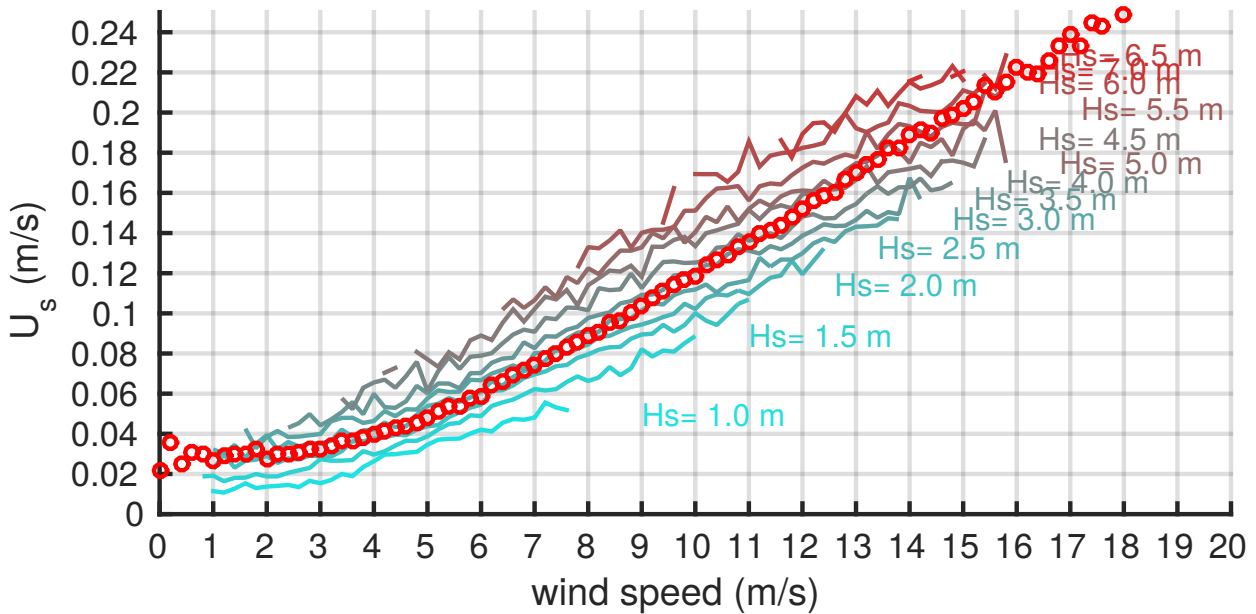

Figure 20: Circles show the mean value of U_s (for a given wind speed), and the colored lines show the mean value of U_s for a given wind speed and wave height. U_s is integrated up to 0.58 Hz. Wave data was obtained from CDIP (station 166, PAPA, maintained by Thomson et al., 2013) and wind measurements at buoy PAPA from OCS Project Office of NOAA/PMEL, wind speed measured at 4.2 m height was averaged over 30 minutes but was NOT corrected to 10 m height. This plot uses 7 years of data from July 2010 to June 2017.

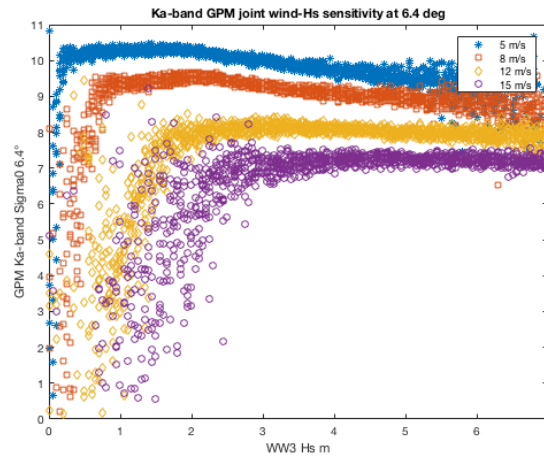Figure 21: Distribution of GPM-derived σ^0 in Ka-band . A few more details are needed here.
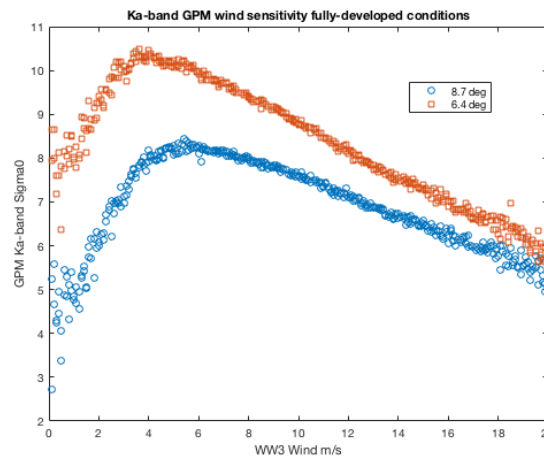

Figure 22: Illustration of the regime change of σ^0 for two incidence angles $\theta = 6.4°$ and $\theta = 8.7°$. Only the data for which the sea state is expected to be fully developed was kept, i.e. $H_s = 0.02\,U^2 \pm 0.05$.

4   Sensitivity of U_{WD} to sea state parameters

The recent analyses by Yurovsky et al. (2019):see section 4.3 discusses this issue, and decomposes the influence of different wave systems to the Doppler measurements, as detailed below. Previous works for other radar frequencies mostly demonstrate that U_{WD} is highly correlated to the wind component in the look azimuth

$$U_{10\parallel} = U_{10}\cos(\varphi_w - \varphi_b) \tag{38}$$

where φ_w is the wind direction and and we recall that φ_b is the radar boresight azimuth. This is particulary discussed by Chapron et al. (2005), who proposed a parameterization of U_{WD} based on $U_{10\parallel}$, with a C-DOP geophysical model function as defined by Mouche et al. (2012) and adapted by Martin et al. (2016) to Ku-band measurements. A similar approach is used by Rodríguez et al. (2018) at higher incidence angles. This is generally based on the fact that both the geophysical velocity, represented by U_s, and the imaging mechanism, related to the root-mean-square ocean slopes, are strongly correlated with the wind speed (Ardhuin et al., 2009; Cox and Munk, 1954). However, this expected high correlation may not give an accurate enough prediction. For example, the correlation coefficient between the 30-minute average wind speed and U_s is $r = 0.86$ at station PAPA (for other examples, see Clarke and Gorder, 2018). Still, for a fixed wind speed the sea state varies and leads to standard deviations of U_S of 60% for wind speed under 5 m/s and this standard deviation goes below 25% only for wind speeds above 10 m/s.

We recall that, for pure wind-sea conditions, U_s and $\mathrm{mss}_{\mathrm{shape}}$ co-varying with wind speed, between a linear and a quadratic function of the wind speed for U_s, almost logarithmic for $\mathrm{mss}_{\mathrm{shape}}$ (Vandemark et al., 2004; Nouguier et al., 2016). As a result, the magnitude M_{WD} of the wave Doppler in Ka-band, solely related to the local wind sea state, should be relatively "flat" as a function of wind speed, and well constrained using $\mathrm{mss}_{\mathrm{shape}}$. The latter can then be directly estimated from co-located SKIM σ^0 measurements. As such, the wind-sea part of M_{WD} can well be considered as a background velocity, an effective short-scale slope velocity Chapron et al. (2004), of order O(1.5 m/s) for light to moderate wind conditions. To note, the Ka-band resonant Bragg scattering scale at $12°$ is about 2 cm, around the capillary-gravity wave transition, corresponding to the minimum phase velocity of about 23 cm/s.

Departure from this background mean-wind relationship between Ka-band σ^0 measurements and M_{WD}, are then largely to be attributed to the non-wind sea state (e.g. presence of different swell systems), and the desired surface current contribution. A swell-system contribution will more strongly impart U_S than $\mathrm{mss}_{\mathrm{shape}}$. Following Yurovsky et al. (2019, eq. 16), the residual sea state contribution may be approximated as

$$U_{\mathrm{WD}} = U_{\mathrm{WD,windsea}} + U_{\mathrm{WD,swell}} = \sum_{n=1}^{N} \beta_n \cdot \mathrm{Re}\left[G_Y M\left(\theta, \varphi_b - \varphi_n, U_{10}\right)\right](AK_n)^2 C_{p,n}, \tag{39}$$

where n represents the n-th out of N wave system, Re is the real part, ϕ_n is the nth-wave-system mean direction, AK_n and $C_{p,n}$ are the steepness and peak phase velocity, respectively. This sum is a natural way to reduce the number of degrees of freedom in the full wave spectrum $E(k, \varphi)$ to a smaller number of meaningful parameters (Gerling, 1992; Portilla et al., 2009). Here G_Y is the geometrical coefficient projecting wave orbital velocity onto the horizontal plane[1], and M is the complex MTF, possibly consisting of tilt M_T and hydro M_H MTFs,

$$M = M_T + M_H = \mathrm{i}M_T\cos(\varphi_b - \varphi_n) + \mathrm{Re}(M_H) + \mathrm{i}\,\mathrm{Im}(M_H), \tag{40}$$

and φ is the radar-to-wave azimuth angle. The coefficient β_N depends on the shape of the spectrum and differs between broad and narrow swell spectra. Key is that these non-local wave systems correspond to large scale background wave systems. Accordingly, these contributions will spread over the SKIM swath, and will be directly estimated from different SKIM measurements, i.e. from the highly range-resolved and directional NRCS modulations both the steepness AK and peak velocity C_p will be obtained. From Yurovsky et al. (2019), a typical narrow swell has a $\beta \simeq 1$ as the Stokes drift

---

[1]Note that in Yurovsky et al. (2019) the velocity is projected on the line of sight to give a V line of sight velocity and not a U horizontal component as we do here. The G parameter of Chapron et al. (2005) corresponds to the product $G_Y M$.

is $(AK)^2 C$. For example, with $C_p = 22$ m/s for a period of 14 s, and $AK \simeq 0.014$ (swell height of 2 m), a tilt MTF $M_T = \partial \sigma^0 / \partial \theta / \sigma^0 \simeq 5$ and $G_Y \simeq \mathrm{i} / \tan \theta$ gives $M_{WD} = 10$ cm/s for $\theta = 12°$.

To gain further understanding to assess the local and non-local wave system contributions, a global brute-force evaluation can be performed. In the context of SKIM near-nadir observations, hydro-MTF contributions may, to first order, be considered small compared to tilt-MTF contributions. Accordingly, a Kirchhoff Approximation (KA) using Gaussian statistics can be used to get a numerical estimation of combined NRCS and mean Doppler frequency shift as a function of any realistic directional wave energy spectrum. Using notations of Nouguier et al. (2018), the Normalized Radar Cross Section writes

$$\sigma^0 = \frac{1}{\pi} \frac{|\mathscr{K}|^2}{(2K)^2} \sec^2(\theta) \zeta^0, \tag{41}$$

and the Doppler pulsation is

$$\omega_D = -\mathrm{i} \partial_\tau \zeta^0 / \zeta^0 \tag{42}$$

with

$$\zeta(\tau) = \int_A \mathrm{e}^{\mathrm{i}\mathbf{Q_H} \cdot \xi} \mathrm{e}^{-Q_z^2 (\rho(0,0) - \rho(\xi,\tau))} \mathrm{d}\xi. \tag{43}$$

and where superscript ^{0} means taken at $\tau = 0$. We have denoted $\mathbf{K_0}$ and $\mathbf{K}$, the incident and scattered EM wave vectors, with their respective horizontal $\mathbf{k_0}$, $\mathbf{k}$ and vertical $-q_0$, q components. One has $\mathbf{K_0} = \mathbf{k_0} - q_0 \hat{\mathbf{z}}$ and $\mathbf{K} = \mathbf{k} + q\hat{\mathbf{z}}$, with positive q and q_0 given by $k_0^2 + q_0^2 = k^2 + q^2 = K_0^2$. $\mathbf{Q_H} = \mathbf{k} - \mathbf{k_0}$ and $Q_z = q + q_0$ are respectively the horizontal and vertical components of the Ewald vector. ρ is the spatio-temporal surface elevation correlation function whose expression writes:

$$\rho(\xi, \tau) = \int_{\mathbb{R}^2} d\mathbf{k} \left[S_d(\mathbf{k}) \mathrm{e}^{-\mathrm{i}\omega\tau} + S_d^*(-\mathbf{k}) \mathrm{e}^{\mathrm{i}\omega\tau} \right] \mathrm{e}^{\mathrm{i}\mathbf{k}\cdot\xi} \tag{44}$$

with $S_d(\mathbf{k})$ being the directional wave energy spectrum and $\omega = \sqrt{gk}$.
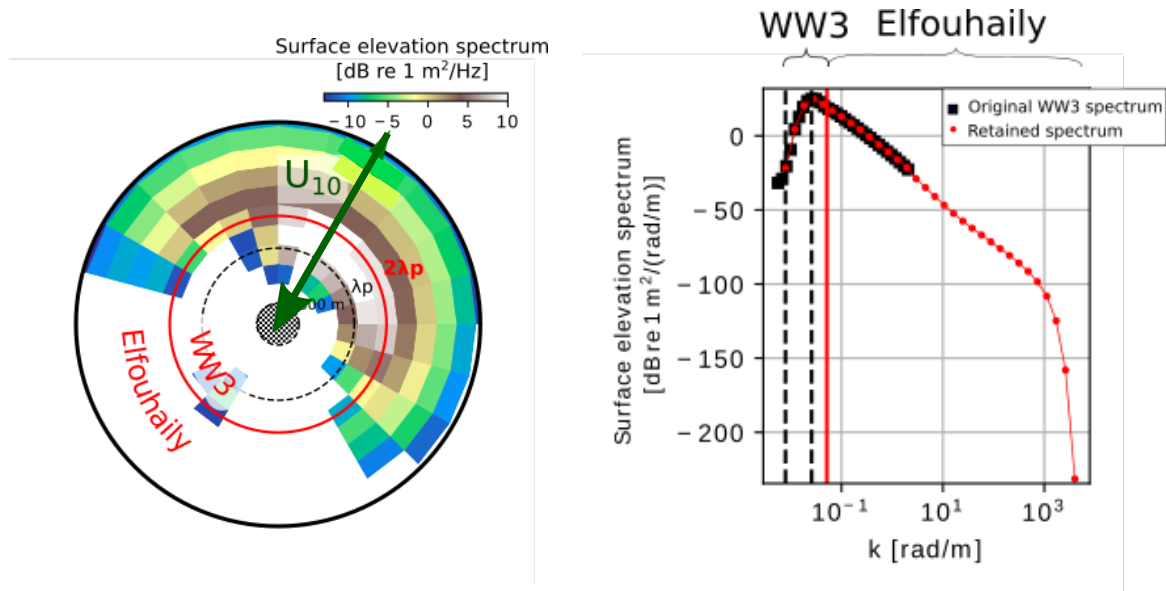

Figure 23: Illustration of the combination of a spectrum from the WAVEWATCH III model with a Elfouhaily spectrum for the short wave components.

For any given input wave spectrum, it is thus possible to obtain U_{WD} using the KA-approximation. Equation (43) is sensitive to the small lag values of ξ and, especially considering Ka-band high-frequency measurements, to the correlation

length of very small waves (« 1 m). It is thus essential to have an accurate description of the small scale part of the wave spectrum, to best constrain the short-scale mean square slope and curvature 2nd order statistical moments (Nouguier et al., 2016). In order to estimate sensitivity of U_{WD} to sea state parameters, we thus rely on a numerical wave model (Ardhuin et al., 2010; Rascle and Ardhuin, 2013) for the wave spectrum up to a cut-off wavelength λ_c of the order of 4 meter, and the use of the spectral description from Elfouhaily (1997) for the shorter components parameterized from the wind speed and direction. From a numerical point of view, the long wave spectrum and the Elfouhaily spectrum are "connected " with a power low junction between k = 1 rad/m (λ = 6.3 m, f = 0.5 Hz) and k = 5 rad/m (λ = 1.25 m, f = 1.12 Hz). Equations (44) and (42) are computed as well as M_{WD}. See figure 23 To be updated with overlap scale as in new version of code?
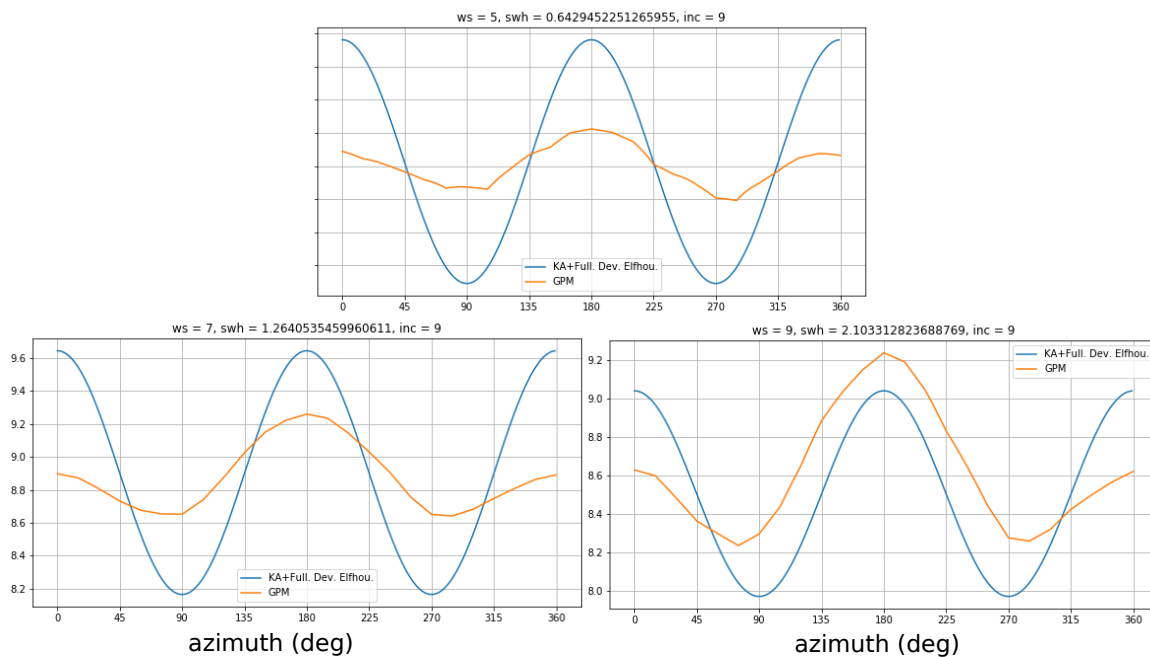

Figure 24: Examples of modeled an climatological variation of σ^0 with the azimuth φ, for low (top) and average wind speeds (bottom) at $\theta = 9°$.

The model is verified to give realistic variations of σ^0 (Fig. 24), with the exception of the upwind / downwind asymmetry, so that the imaging mechanism is expected to be well represented, giving correct orders of magnitude for the geophysical Doppler. To quote Cox and Munk (1954) and further reviewed (Chapron et al., 2002), there is some skewness (upwind/downwind asymmetry) which increases with increasing wind speed. As a result the most probable slope at high winds is not zero but a few degrees, with the azimuth of ascent pointing downwind. At Ka-band, Walsh et al. (2008) reported a 1° downwind shift at 14 m/s, while Chapron et al. (2002) reported almost 2° for optical glitter measurements. Finally, when comparing model results and global satellite observations, (Fig. 24), it must be understood that instrument noise, unavoidable effects of fluctuating environmental conditions, as well as imperfect model estimates, cause random effects which show up in any direct observational scatter, to often lead to systematic biases. In particular, reported directional modulations are likely to be underestimated from the global satellite analysis.

Using the KA-framework, figure 25 shows a variation from 2 m/s to 3 m/s between 5 m/s to 20 m/s wind speed. The values obtained $M_{\text{WD}} \simeq 2.4$ m/s at 8 m/s, is 38 times a mean Stokes drift of 0.08 m/s. This is broadly consistent with the analysis of Ka-band σ^0, with a typical value of 1.9 m/s (Yurovsky et al., 2017; Yurovsky et al., 2019), including non-negligible swell contributions. Such a difference in magnitude suggests that the true M_{WD} variability will have to be learned from data, similar to what has been previously proposed by Rodríguez et al. (2018) or Martin et al. (2018), except that we will use more parameters than just the wind speed, i.e. wave age and wind rotation that affect the local wind sea and non-local swell system contributions.
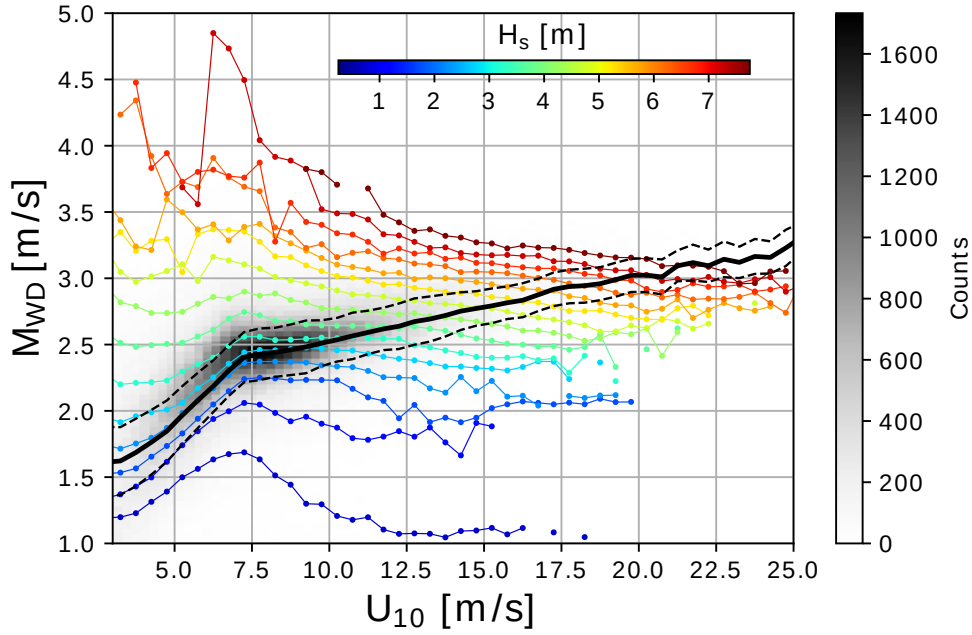

Figure 25: Computed variability of the wave Doppler magnitude M_{WD} for a wide range of modeled ocean wave spectra, plotted here as a function of the wind speed. The colored curves show the median value for different classes of wave height for a given wind speed, each curve is separated by 0.5 m.

In order to reduce the number of degrees of freedom contained in the full sea state spectrum, we have sought to explain the variability of U_{WD} or M_{WD} with a limited set of parameters that are integrals ("moments") of the wave spectrum. Guided by the analysis above we have worked with different sets of parameters.

4.1   Moments of the wave spectrum

Considering a limited wavenumber range from k_1 to k_2 we define, the contribution of one direction (i.e. one cycle of measurements) to the Stokes drift

$$U_{S,1D}(k_1, k_2, \varphi) = \int_{k_1}^{k_2} 2\sqrt{g} k^{1.5} E(k, \varphi) \mathrm{d}k \tag{45}$$

similarly, the local contribution to the mss is

$$\text{mss}_{1D}(k_1, k_2, \varphi) = \int_{k_1}^{k_2} k^2 E(k, \varphi) \mathrm{d}k \tag{46}$$

and a local contribution to the orbital velocity variance is

$$E_{U,1D}(k_1,k_2,\varphi) = \int_{k_1}^{k_2} gkE(k,\varphi)\mathrm{d}k \tag{47}$$

and the contribution to the surface elevation

$$E_{1D}(k_1,k_2,\varphi) = \int_{k_1}^{k_2} E(k,\varphi)\mathrm{d}k \tag{48}$$

From these, we can integrate in azimuth (over different cycles) to obtain the corresponding Stokes drift in azimuth φ

$$U_S(k_1,k_2,\varphi) = \int_0^{2\pi} U_{S,1D}(k_1,k_2,\varphi')\cos(\varphi-\varphi')\mathrm{d}\varphi' \tag{49}$$

a slope variance in direction φ

$$\mathrm{mss}(k_1,k_2,\varphi) = \int_0^{2\pi} \mathrm{mss}_{1D}(k_1,k_2,\varphi')\cos^2(\varphi-\varphi')\mathrm{d}\varphi' \tag{50}$$

and a velocity variance in direction φ

$$E_U(k_1,k_2,\varphi) = \int_0^{2\pi} E_{U,1D}(k_1,k_2,\varphi')\cos^2(\varphi-\varphi')\mathrm{d}\varphi' \tag{51}$$

From these one can obtain the norm $U_S(k_1,k_2) = \sqrt{U_S^2(k_1,k_2,\varphi) + U_S^2(k_1,k_2,\varphi+\pi/2)}$, and a partially-integrated wave height

$$H_s(k_1,k_2) = 4\sqrt{\int_0^{2\pi} E_{1D}(k_1,k_2,\varphi')\mathrm{d}\varphi'} \tag{52}$$

4.2 Results with a first set

Here we have used the range of our wave model simulations, namely $k_2 = 0.0055$ rad/m, $k_2 = 1.97$ rad/m, and the five parameters are, U_{10}, $\min(U_{10}, 8\,\mathrm{m/s})$, $U_S(k_1,k_2)$,H_s, mss. Figure 26 shows the residual error statistics when using one or a few parameters. The variation of M_{WD} as a function of the 5 parameters was learnt on a training dataset of around 6,000,000 spectra coming from a wide range of situations. The fitting procedure uses a softmax function to model the U_{WD} likelihood.

4.2.1 The Softmax method description

The goal of this method is to extract the likelihood of given measure y (here y can have more than one dimension) from a vector x. The method aims to compute the log likelihood using simplified Softmax (expecting that sum of the likelihood is equal to one). Thus, the probability to have $y = k$ at the level k can be written as

$$ln\left(P(y=k|\Theta)\right) = \sum_i W_{k,i}\Theta + b_k \tag{53}$$

4.2.2 Learning method

Having a set of x related to a known corresponding y PDF, a linear regression for each value of k provide the $W_{k,i}$ and b_k. In the case where the log likelihood is not known, but just the most probable value we build a learning likelihood

$$\log\left(P(y_i=k|\Theta)\right) = -\frac{k-k_i^2}{2\sigma^2}. \tag{54}$$

It is again a linear regression. The σ prior can be iterated to improve the performance of the retrieval on the learning database.
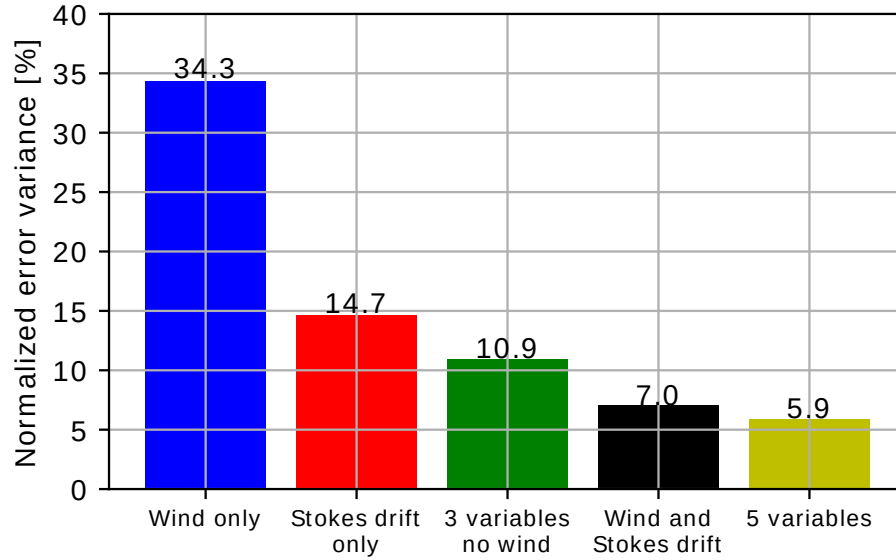
Figure 26: Root mean square error on M_{WD} when using different combination of variables. The 3 variables used without wind are H_s, U_s and "mss": this "mss" is actually a mss_{long} obtained from the model integrated up to 0.72 Hz, similar to the values in Vandemark et al. (2004).

4.3 Results with a second set

Instead of parameterizing M_{WD} we may directly parameterize U_{WD} use the radial Stokes drift U_S as

$$U_{\text{WD}} = GU_S \tag{55}$$

where G is parameterized from additional parameters, namely $\text{mss}(k_2)$, U_{10}, H_s ...

5 Splitting $U_{GD}(\varphi)$ in $U_{WD}(\varphi) + U_{CD}(\varphi)$ using SKIM, MetOp and other data

Based on the sensitivity analysis above, we may use most of the available parameters and recombine them. After listing all the useful parameters and their error model, we describe two approaches for splitting U_{GD} into U_{WD} and U_{CD}. The first approach is deterministic and is applied for each cycle separately, using data from other cycles that may be located at relatively large distances. This follows Ardhuin et al. (2018), now considering ambiguous and noisy wave spectra. .

The second approach is stochastic and assumes smoothly varying fields, so that a single value of $U_{CD}(0)$ and $U_{CD}(\pi/2)$ is estimated for a given "box", in which multiple cycles are present, see figure 4. That second approach generalizes the work of Martin et al. (2018) to a Ka-Dop GMF that is a function of the wind vector, here replaced by the Stokes drift vector, and also other parameters.

5.1 Relevant measurements

5.1.1 Nadir data

Sea state parameters on the nadir beam include at least

- the significant wave height H_s, with an accuracy ...

- the backscatter coefficient σ_0 that can be related to a mss_{shape} (Vandemark et al., 2004; Nouguier et al., 2016)

- Along-track H_s and σ_0 gradients

- other moments of the wave spectrum, using the L1A stack data (to be discussed later)

5.1.2 6 deg. beams

Here we have

- the backscatter coefficient σ_0 that can be related to a mss_{shape}

- the mean Doppler velocity U_{GD}

- the backscatter modulation spectrum $E_b(k, \varphi)$ with 180 deg. ambiguity and an error model given by ...

We expect that the modulation spectrum is related to the slope spectrum via a modulation transfer function that combines both range bunching (Jackson, 1987) and tilt effects (Nouguier et al., 2018).

5.1.3 12 deg. beams

- the backscatter coefficient σ_0 that may be be related to a mss_{shape} but with a weaker variability than at other incidence angles

- the mean Doppler velocity U_{GD}

- the backscatter modulation spectrum $E_b(k, \varphi)$ with 180 deg. ambiguity and an error model given by ... We expect that the modulation spectrum is related to the slope spectrum via a modulation transfer function that is weakly affected by range bunching (Jackson, 1987) but dominated by tilt effects (Nouguier et al., 2018).

5.1.4 MetOp data

- SCA Wind speed U_{10} and direction φ_{wnd}, this is used in the first approach as a first guess to disambiguate the wave spectrum, as shown in figure 27.

- The SCA σ^0 may be used directly in the cost function for a joint inversion of wind, waves and current.
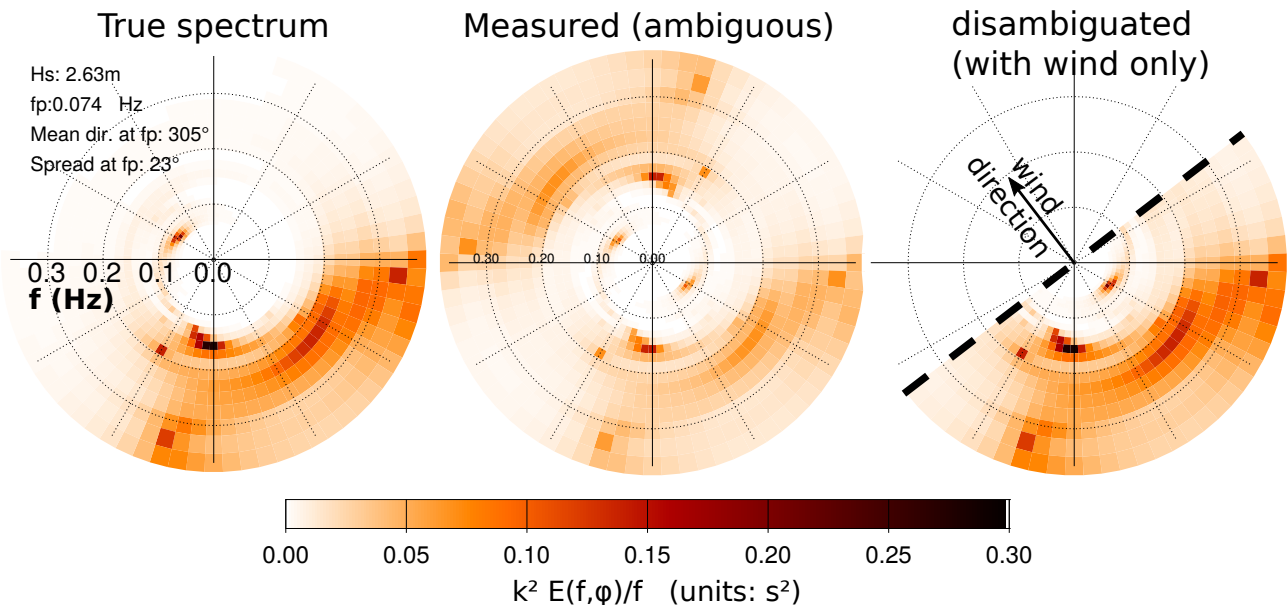
Figure 27: Example of wave spectrum $E(f, \varphi)$ converted to surface slopes, and ambiguity removal using the wind direction. in practice the wind direction is given by MetOp SCA or, when not available by a NWP model such as ECMWF. This particular spectrum corresponds to the 22 November 2018 case observed during the DRIFT4SKIM campaign . Instead of using only wind, we expect to use the co-spectrum of Doppler and σ^0 where the SNR is large enough, this should allow to put the swell peaks in the right direction, and possibly determine the amount of energy travelling in opposite directions, which is needed for the secondary SKIM objective of microseism sources (Ardhuin et al., 2011). Note that the directional resoltion in this plot is $5°$, which is finer than the resolution obtained with a single beam, but coarser than the resolution achievable by optimizing the angular diversity of the different beams, as shown in figure 4.

5.2   Deterministic inversion from modeled data

This approach uses the functional form of U_{WD} described above and the goal is thus to estimate all the necessary parameters at the location of each cycle. For the ancillary data (wind speed and direction from MetOp SCA or a NWP model) this is obtained by interpolation at the footprint center.

For the moments listed in section 4.1, we should be careful that the $6°$ and $12°$ beams may require a different range of integration $[k_1, k_2]$ due to a different noise floor and different MTFs. Also the spectra error can be particularly large in uptrack and down-track directions.

Add details here and figure with noisy spectrum: Charles

As a result we will exclude modulation data in a sector of $\pm 8°$ (TBC) around the uptrack and down-track directions, interpolating from the neighboring directions. Here are some of the steps followed to compute any of these moments,

- Compute PSDs following Welch (1967), excluding segments with NV > 1.4 (TBC), using 4 + 3 half-overlapping windows (using more than that gives a poor spectral resolution for swell, at 12 deg, and waves of 0.1 Hz the frequency resolution is 0.0041, comparable to typical Datawell buoy settings. This means doing FFTs over 512 points. This is done in the Level 1B to level 2A_WR processing

- Remove a noise floor

- Apply MTF on level 2A_WR σ^0 spectrum

- Remove directional ambiguity using wind (for high frequency) or co-spectrum (for swell peaks). This gives the Level 2B_WDS spectrum.

- Integrate over k from k_1 to k_2, to produce X_{1D} moments

- Sum the 1D moments from the nearest c_n cycles, with $-11 < n < 11$ in the case of $N_\varphi = 45$ used here. The selection of cycles may be perturbed by flagging (rain, low wind, coast, ice edge, uptrack/downtrack), and we reserve the possibility to interpolate across a $\approx 20°$ gap (in particular for the uptrack/dowtrack directions). We note that the half-width of the wind sea peak is typically 30 deg so we have a bit of room.
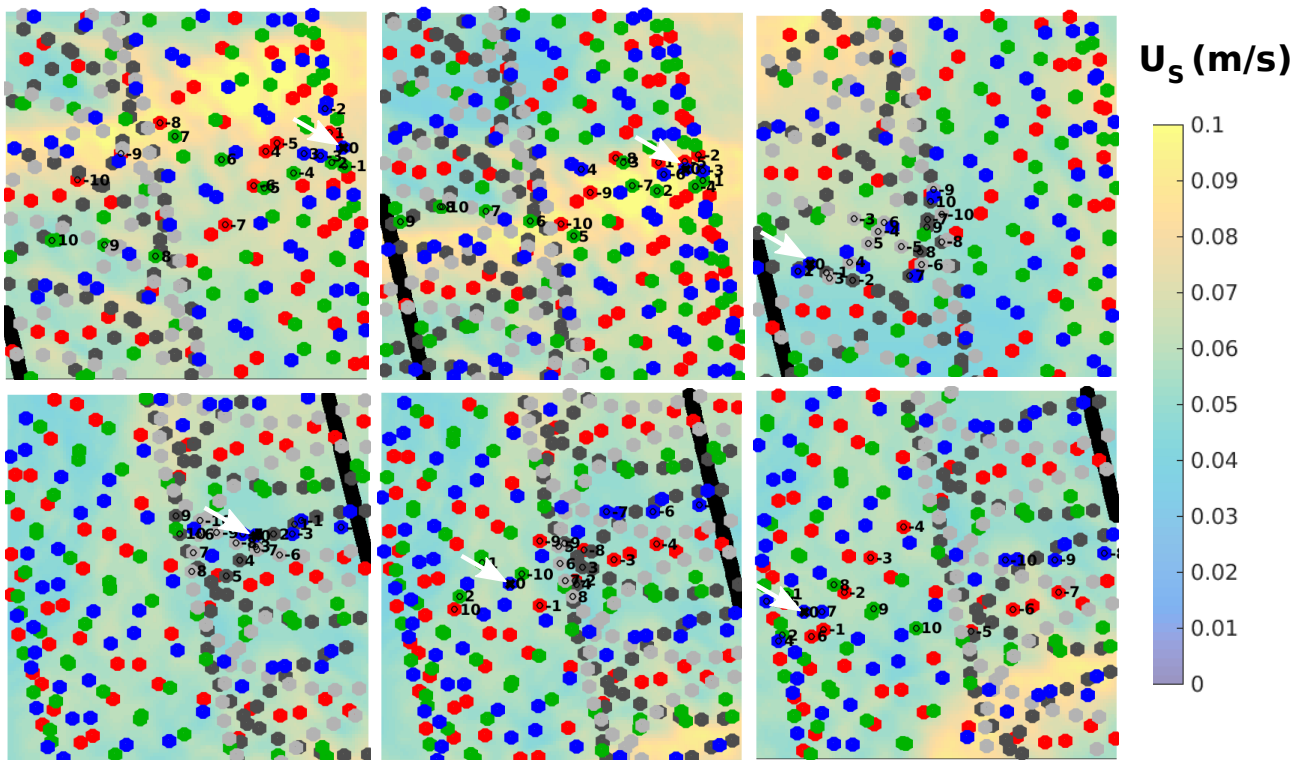

Figure 28: Example of cycles φ' (numbered -11 to +11), used in the directional sum for obtaining directional moments at the cycle of interest with direction φ, labeled 0, at the location of the white arrow. The background in the map of Stokes drift magnitude U_S, this is an example in the Gulf Stream where strong gradients of the sea state are caused by the strong current and the relatively short wave period.

The sum over the other cycles of azimuth φ' includes azimuths between $\varphi - \pi/2$ and $\varphi + \pi/2$ or $\varphi + \pi - \pi/2$ and $\varphi + \pi + \pi/2$ because both φ' and $\varphi' + \pi$ are observed in the same cycle φ'. As shown in Figure 28, the cycles used in the sum are spread out over half of the swath, i.e. 150 km, when the sum is made at the outer edge of the swath. This is because the only place in the swath that has along-track directions is in the center.

For those directional moments that are weighted by $\cos(\varphi - \varphi')$ or $\cos^2(\varphi - \varphi')$ the contributions from very oblique angles are marginal. Still, the indices ± 7 are only separated by $56°$, where $\cos(\varphi - \varphi')$ is still 0.5.
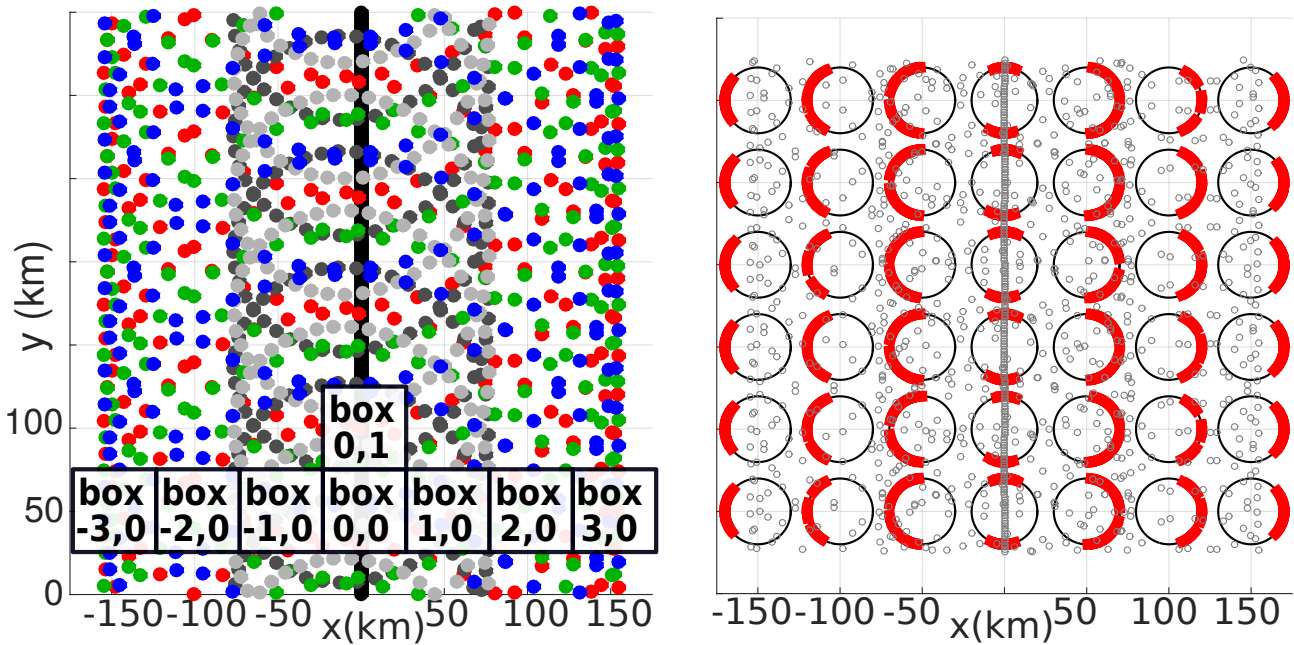

Figure 29: Left: sampling patters of the different beams. Right: Range of look azimuths for cycles in a 50 by 50 km box. For each box, the thin circle shows all possible azimuths, and the red sectors are the one sampled within the box.

As a result, any large spatial gradient will lead to large errors in the estimation of moments, in particular for along-track waves and for the outer part of the swath. This is a particular problem near coasts, or ice edge aligned along the track.

Ardhuin et al. (2018) estimated that the error on the radial Stokes drift $U_S(\varphi)$ that is associated to the spatial gradients of U_S could be parameterized as a function of the variability on the Stokes drift magnitude over the entire swath, denoted $\text{std}(U_S)$ and the root mean square distance r_2 of the contributing cycles weighted by the cosine of the angle difference,

$$\text{err}(U_S) \simeq \varepsilon \text{std}(U_S) \frac{r_2}{20\text{km}} \tag{56}$$

with ε of the order of 0.15. This error parameterization is for a whole swath region and it does not distinguish between cycles that are well approximated and others. The end result, with $G = 25$, is a rms error of the order of 8 cm/s in the Gulf stream region when then mean Stokes drift is of the order of 6 cm/s.

Preliminary analysis suggest that it is possible to automatically learn the expected variations of spectral properties and use a sparse set of observations (without the full spectrum) to reconstruct maps of spectral moments at higher resolution that the 150 km size box necessary to gather all the directional component. JMD: some comments to be added here, if possible, with a couple of plots.
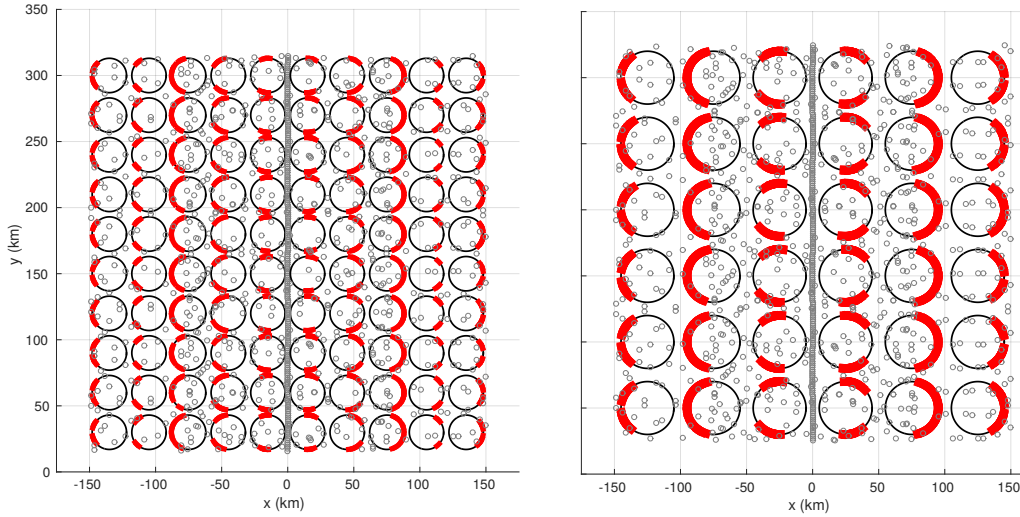
centering

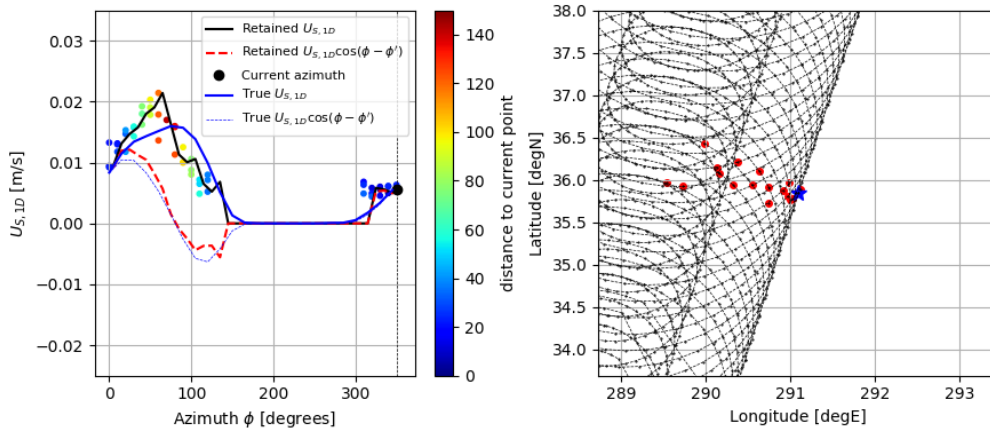Figure 30: Things change a little when the boxes are shifted or made smaller.

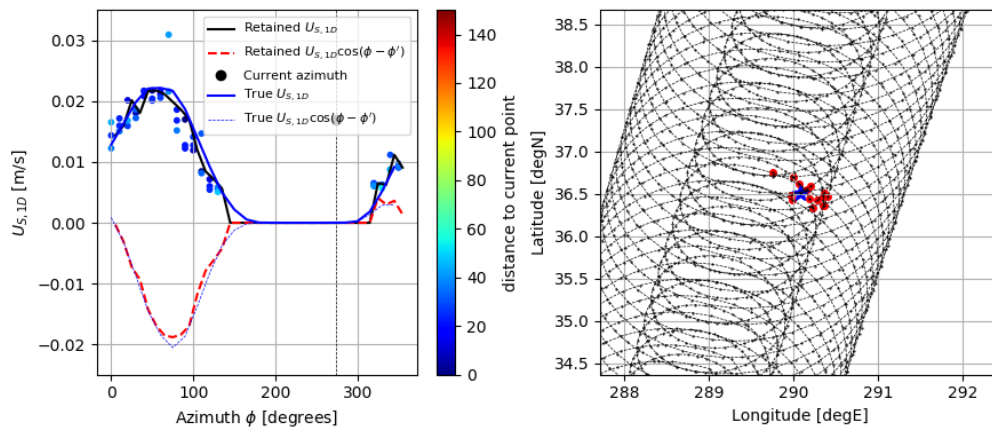Figure 31: Example of a sum of $U_{S,1D}$ contribution from different cycles.

Figure 32: Example of a sum of $U_{S,1D}$ contribution from different cycles.

5.3   Learning approach (GMF) based on data

The deterministic approach outlined above relied on a GMF expressing U_{WD} as a function of a number of sea state parameters. Here this GMF was learned on simulated data. With real SKIM data, we can use the near-nadir and near-6deg boxes to learn the GMF.

5.4   Stochastic inversion from modeled data

Contrary to the previous approach we will consider here the inversion from data constrained to a given box, relaxing the requirement on the quality of the data if necessary. The stochastic part is particularly suited to the cases in which a single measurement, or combination of measurements, can correspond to two or more ambiguous parameters to be estimated. This is generally the case of σ^0 as shown in the figure 21, and for multi-direction scatterometer data. To be further described in version 2 of this note.

This generalizes the approach of Martin et al. (2018), applied to a "box" in which the current components $U_{CD,x}$ an $U_{CD,y}$ vary smoothly, with a Ka-DOP GMF for the geophysical Doppler that is not just a function of wind speed but also a function of the sea state (wave age and swell). We expect to have a cost function that is the sum of a Doppler term (misfit of Ka-DOP and measured Doppler), a σ^0 term, with a σ^0 GMF to be fitted to the data in the box, i.e. nadir and/or $6°$ beams and/or $12°$, and a wave modulation term, related to the same spectral moments that get into the Ka-DOP GMF. Finally a regularization term may be added to require smoothness between boxes and the algorithm may be applied in a "pyramidal search" way, starting with big boxes and finishing with 15 to 30 km size boxes.

6   Error budget

To be completed soon. Basically, for Level 2B we have

- the instrument phase error, around 15 cm/s times $\sin(\varphi - \varphi_t)$

- the σ^0 gradient error, of the same order of magnitude also with a $\sin(\varphi - \varphi_t)$ dependency

- the Wave Doppler residual around 20 cm/s

This is then integrated in "boxes" for Level 2C with additional "Dilution of Precision" on some components (i.e. cross-track is poor near nadir, along-track is poor in the outer part of swath), and mapping error, but the benefit of averaging ten or more individual L2B measurements into a L2C data point.

A Pulse-Pair signal and non-geophysical Doppler

The raw pulse-pair signal in range cell r results from an integration of infinitesimal contributions scattered from the circular ring of the sea surface located at distance r from the radar. In the frame of reference of the rotating Earth, the complex measured signal is (e.g. Rodríguez et al., 2018)

$$PP(r,t) = C(r) \int G(\theta, \varphi) e^{-i\frac{4\pi}{\lambda} \Delta t V_{\text{geo}} - V_o} \sigma^0(x, y, \theta, \varphi) d\varphi \tag{A.1}$$

where $C(r)$ is a r-dependent factor describing the amplitude variation of the pulse-pair signal due to spherical spreading and instrument factors such as transmitted power or electronic or processing gains, λ is the electromagnetic wavelength, and Δt is the time separation of the two radar pulses considered, $G(\theta, \varphi)$, the two-way antenna gain, V_{geo} is the geometric velocity of the radar projected on the line of sight, as given by eq. 10, and V_o is the similar projection of the surface velocity (Nouguier et al., 2018).

The horizontal position on the sea surface (x, y) is assumed to be uniquely related to the angles (θ, φ), so that variations of σ^0 as a function of φ are observed as an apparent variation as a function of (x, y).

For an airborne system we can neglect the curvature of the Earth surface and θ is equal to the elevation angle of the radar pointing, and $\cos\theta = H/r$, with H the flight altitude (Figure 1).

PP(r,t) = C(r) Eq. (A.1 can be expressed as a cumulant expansion, leading to,

$$PP(r,t) \simeq C(r) \exp\left[-i\frac{4\pi\Delta t}{\lambda}\kappa_1 - \frac{16\pi^2\Delta t^2}{\lambda^2}\frac{\kappa_2}{2} + \cdots\right],$$

with

$$\kappa_1 = \frac{\int (V_{\text{geo}} - V_o) G(\theta, \varphi) \sigma^0(\theta, \varphi) d\varphi}{\int G(\theta, \varphi) \sigma^0(\theta, \varphi) d\varphi}$$

and

$$\kappa_2 = \frac{\int (V_{\text{geo}} - V_o)^2 G(\theta, \varphi) \sigma^0(\theta, \varphi) d\varphi}{\int G(\theta, \varphi) \sigma^0(\theta, \varphi) d\varphi} - \kappa_1^2.$$

It is easy to see that κ_1 is linked to the phase of $PP(r)$, while κ_2 introduces a correction to the amplitude of $PP(r)$. **V** does not vary with θ and φ. κ_1 can thus be expressed as,

$$\kappa_1 = \frac{\int V_o G(\theta, \varphi) \sigma^0(\theta, \varphi) d\varphi}{\int G(\theta, \varphi) \sigma^0(\theta, \varphi) d\varphi} - V_{\text{geo}}(\theta + \varepsilon, \varphi + \delta), \tag{A.2}$$

with the apparent mispointing angles ε and δ such that the unit vector along the line of sight, with $\varphi = 0$ corresponding here to the along-y axis direction, and the directions are counted clockwise,

$$\mathbf{e}(\theta, \varphi) = (\sin\theta\sin\varphi, \sin\theta\cos\varphi, \cos\theta) \tag{A.3}$$

integrates to an apparent line of sight

$$\mathbf{e}_{\text{eff}} = \frac{\int \mathbf{e}(\theta, \varphi') G(\theta, \varphi') \sigma^0(\theta, \varphi') d\varphi'}{\int G(\theta, \varphi') \sigma^0(\theta, \varphi') d\varphi'} \tag{A.4}$$

of incidence $\theta + \varepsilon$ and azimuth $\varphi + \delta$.

In practice we may consider that $|V_o| \ll |V_{\text{geo}}|$. We further consider weak variations of σ^0 across the beam so that the integrand can be expanded around $\varphi' - \varphi$, and the linear variation of the projection along $\mathbf{e}$ correlates with the linear trend of σ^0. A narrow Gaussian antenna pattern writes $G \propto \exp(-(\phi - \phi_b)^2/2\alpha^2)$, ϕ being the relative angle between the slant range vector and the boresight vector. With $(\phi - \phi_b) = (\varphi - \varphi_b)\sin\theta$, we have

$$\frac{\int_{-\infty}^{\infty} (\varphi' - \varphi)^2 G d\varphi'}{\int_{-\infty}^{\infty} G d\varphi'} = \frac{\alpha^2}{\sin^2\theta}. \tag{A.5}$$

This gives the following correction to the line of sight velocity

$$V_\delta = \frac{\alpha^2}{\sin\theta} \frac{1}{\sigma^0} \frac{\partial \sigma^0}{\partial \varphi} (V_x \cos\varphi - V_y \sin\varphi)$$

which is equivalent to a change due to a mispointing given by eq. (13).

A more generic variation of σ^0 associated to spatial gradients may contain fast variations within the footprint, proportional to $\sin\beta\varphi$. Given that

$$\frac{\int_{-\infty}^{\infty}[1+\varepsilon\sin(\beta(\varphi'-\varphi))](\varphi'-\varphi)Gd\varphi'}{\int_{-\infty}^{\infty}[1+\varepsilon\sin(\beta(\varphi'-\varphi))]Gd\varphi'}$$
$$= \frac{\varepsilon\alpha^2\beta}{\sin^2\theta}\exp(-\beta^2\alpha^2/2\sin\theta^2). \tag{A.6}$$

we get the apparent mispointing given by eq. (16). We can thus use a Fourier decomposition of the spatial patterns of σ^0 to estimate the apparent mispointing when these patterns are at scales comparable to the antenna footprint.

B Spherical-Earth expressions for θ and γ

The spacecraft S is at altitude h above the Earth surface. R_e is the radius of the Earth. S is thus at distance $h + R_e$ from the Earth center C. The observation point P is located at distance R from S, and is at height δP above the spherical Earth surface. Then θ, the angle SP makes with SC, can be expressed as:

$$\theta = \arccos\left[\frac{(h-\delta P)+(h^2+R^2-\delta P^2)/(2R_e)}{R(1+h/R_e)}\right].$$

Meanwhile, γ, the angle SP makes with PC, can be expressed as:

$$\gamma = \arccos\left[\frac{(h-\delta P)+(h^2-R^2-\delta P^2)/(2R_e)}{R(1+\delta P/R_e)}\right].$$

Clearly, these expressions coincide in the flat-Earth limit $R_e \to \infty$.

Bibliography

Ardhuin, F., L. Marié, N. Rascle, P. Forget, and A. Roland (2009). "Observation and estimation of Lagrangian, Stokes and Eulerian currents induced by wind and waves at the sea surface". In: *J. Phys. Oceanogr.* 39(11), pp. 2820–2838. DOI: 10.1175/2009JPO4169.1. URL: http://journals.ametsoc.org/doi/pdf/10.1175/2009JPO4169.1.

Ardhuin, F., E. Rogers, A. Babanin, J.-F. Filipot, R. Magne, A. Roland, A. van der Westhuysen, P. Queffeulou, J.-M. Lefevre, L. Aouf, and F. Collard (2010). "Semi-empirical dissipation source functions for wind-wave models: part I, definition, calibration and validation". In: *J. Phys. Oceanogr.* 40(9), pp. 1917–1941. DOI: 10.1175/2010JPO4324.1.

Ardhuin, F., E. Stutzmann, M. Schimmel, and A. Mangeney (2011). "Ocean wave sources of seismic noise". In: *J. Geophys. Res.* 116, p. C09004. DOI: 10.1029/2011JC006952. URL: http://wwz.ifremer.fr/iowaga/content/download/48407/690392/file/Ardhuin_etal_JGR2011.pdf.

Ardhuin, F., N. Rascle, B. Chapron, J. Gula, J. Molemaker, S. T. Gille, D. Menemenlis, and C. Rocha (2017). "Small scale currents have large effects on wind wave heights". In: *J. Geophys. Res.* 122(C6), pp. 4500–4517. DOI: 10.1002/2016JC012413.

Ardhuin, F., Y. Aksenov, A. Benetazzo, L. Bertino, P. Brandt, E. Caubet, B. Chapron, F. Collard, S. Cravatte, F. Dias, G. Dibarboure, L. Gaultier, J. Johannessen, A. Korosov, G. Manucharyan, D. Menemenlis, M. Menendez, G. Monnier, A. Mouche, F. Nouguier, G. Nurser, P. Rampal, A. Reniers, E. Rodriguez, J. Stopa, C. Tison, M. Tissier, C. Ubelmann, E. van Sebille, J. Vialard, and J. Xie (2018). "Measuring currents, ice drift, and waves from space: the Sea Surface KInematics Multiscale monitoring (SKIM) concept". In: *Ocean Sci.* 14, pp. 337–354. DOI: 10.5194/os-2017-65.

Barrick, D. E., J. M. Headrick, R. W. Bogle, and D. D. Crombie (1974). "Sea backscatter at HF: interpretation and utilization of the echo". In: *Proc. IEEE* 62, p. 673.

Battaglia, A., K. Mroz, D. Watters, and F. Ardhuin (submitted). "GPM-derived climatology of attenuation due to clouds and precipitation at Ka-band". In: *IEEE Trans. on Geosci. and Remote Sensing*.

Bréon, F. M. and N. Henriot (2006). "Spaceborne observations of ocean glint reflectance and modeling of wave slope distributions". In: *J. Geophys. Res.* 111, p. C0605. DOI: 10.1029/2005JC003343.

Chapron, B., V. Kerbaol, D. Vandemark, and T. Elfouhaily (2000). "Importance of peakedness in sea surface slope measurements". In: *J. Geophys. Res.* 105(C7), pp. 17195–17202.

Chapron, B., F. Collard, and V. Kerbaol (2004). "Satellite synthetic aperture radar sea surface Doppler measurements". In: *Proceedings of 2nd workshop on Coastal and Marine Applications of Synthetic Aperture Radar, Svalbard, 8-12 sep, 2003*. ESA SP-565. ESA Publication Division, pp. 133–141.

Chapron, B., D. Vandemark, and T. Elfouhaily (2002). "On the skewness of the sea slope probability distribution". In: *Gas transfer at water surfaces*. Ed. by M. A. Donelan, W. M. Drennan, E. S. Saltzman, and R. Wanninkhof. Vol. 127. Geophys. Monogr. Ser. American Geophysical Union, pp. 59–63. DOI: 10.1029/GM127p0059.

Chapron, B., F. Collard, and F. Ardhuin (2005). "Direct measurements of ocean surface velocity from space: interpretation and validation". In: *J. Geophys. Res.* 110(C07008). DOI: 10.1029/2004JC002809.

Chelton, D. B., E. J. Walsh, and J. L. MacArthur (1989). "Pulse compression and sea level tracking in satellite altimetry". In: *J. Atmos. Ocean Technol.* 6, pp. 407–438. DOI: 10.1175/1520-0426(1989)006<0407:pcaslt>2.0.co;2.

Clarke, A. J. and S. V. Gorder (2018). "The Relationship of Near-Surface Flow, Stokes Drift and the Wind Stress". In: *J. Geophys. Res.* 123, pp. 4680–4692. DOI: 10.1029/2018JC014102.

Cox, C. and W. Munk (1954). "Measurement of the roughness of the sea surface from photographs of the sun's glitter". In: *J. Opt. Soc. Am.* 44(11), pp. 838–850. DOI: 10.1364/josa.44.000838.

Elfouhaily, T., B. Chapron, K. Katsaros, and D. Vandemark (1997). "A unified directional spectrum for long and short wind-driven waves". In: *J. Geophys. Res.* 102(C7), pp. 15781–15796.

Elfouhaily, T. M. (1997). "A consistent wind and wave model and its application to microwave remote sensing of the ocean surface". PhD thesis. Denis Diderot University, Paris.

Gerling, T. W. (1992). "Partitioning sequences and arrays of directional ocean wave spectra into component wave systems". In: *J. Atmos. Ocean Technol.* 9, pp. 444–458. URL: http://ams.allenpress.com/archive/1520-0426/9/4/pdf/i1520-0426-9-4-444.pdf.

Hansen, M. W., F. Collard, K.-F. Dagestad, J. A. Johannessen, P. Fabry, and B. Chapron (2011). "Retrieval of Sea Surface Range Velocities From Envisat ASAR Doppler Centroid Measurements". In: *IEEE Trans. on Geosci. and Remote Sensing* 49(10), pp. 3582–. DOI: 10.1109/TGRS.2011.2153864.

Hauser, D., C. Tison, T. Amiot, L. Delaye, N. Corcoral, and P. Castillan (2017). "SWIM: The First Spaceborne Wave Scatterometer". In: *IEEE Trans. on Geosci. and Remote Sensing* 55(5), pp. 3000–3014.

Jackson, F. C. (1987). "The physical basis for estimating wave-energy spectra with the radar ocean-wave spectrometer". In: *Johns Hopkins APL Technical Digest*. Vol. 8. 1, pp. 70–73.

Jackson, F. C., W. T. Walton, and C. Y. Peng (1985). "A comparison of in situ and airborne radar observations of ocean wave directionality". In: *J. Geophys. Res.* 90(C1), pp. 1005–1018.

Kenyon, K. E. (1969). "Stokes drift for random gravity waves". In: *J. Geophys. Res.* 74, pp. 6991–6994.

Kudryavtsev, V., M. Yurovskaya, B. Chapron, F. Collard, and C. Donlon (2017). "Sun glitter Imagery of Surface Waves. Part 1: Directional spectrum retrieval and validation". In: *J. Geophys. Res.* 122. DOI: 10.1002/2016JC012425.

Kuik, A. J., G. P. van Vledder, and L. H. Holthuijsen (1988). "A method for the routine analysis of pitch-and-roll buoy wave data". In: *J. Phys. Oceanogr.* 18, pp. 1020–1034. URL: http://journals.ametsoc.org/doi/pdf/10.1175/1520-0485%281987%29017%3C0845%3ATROWDT%3E2.0.CO%3B2.

Lillibridge, J., R. Scharroo, S. Abdalla, and D. Vandemark (2014). "One- and Two-Dimensional Wind Speed Models for Ka-Band Altimetry". In: *J. Atmos. Ocean Technol.* 31, pp. 630–638. DOI: 10.1175/JTECH-D-13-00167.1.

Madsen, S. N. (1989). "Estimation the Doppler Centroid of SAR Data". In: *IEEE Trans. on Aerospace and Electronic Systems* AES-25(2), pp. 134–140.

Marié, L., F. Collard, L. Pineau-Guillou, D. Hauser, F. Boy, C. Peureux, and F. Ardhuin (2019). "Measuring ocean surface velocities with the KuROS airborne near-nadir Doppler radar: a multi-scale analysis in preparation of the SKIM mission". In: *Ocean Sci.* in preparation.

Martin, A. C. H., C. Gommenginger, J. Marquez, S. Doody, V. Navarro, and C. Buck (2016). "Wind-wave-induced velocity in ATI SAR ocean surface currents: First experimental evidence from an airborne campaign". In: *J. Geophys. Res.* 121, pp. 1640–1653. DOI: 10.1002/2015JC011459.

Martin, A. C. H., C. P. Gommenginger, and Y. Quilfen (2018). "Simultaneous ocean surface current and wind vectors retrieval with squinted SAR interferometry: Geophysical inversion and performance assessment". In: *Remote sensing of Environment* 216, pp. 798–808. DOI: 10.1016/j.rse.2018.06.013.

Meissner, T. and F. Wentz (2016). "The complex dielectric constant of pure and sea water from microwave satellite observations". In: *IEEE Trans. on Geosci. and Remote Sensing* 42(9), pp. 1836–1849. DOI: 10.1109/lgrs.2016.2520823.

Mouche, A. A., B. Chapron, and N. Reul (2008). "Predicted Doppler shifts induced by ocean surface wave displacements using asymptotic electromagnetic wave scattering theories". In: *Waves in Random and Complex Media* 18(1). DOI: 10.1080/17455030701564644.

Mouche, A., F. Collard, B. Chapron, K.-F. Dagestad, G. Guitton, J. A. Johannessen, V. Kerbaol, and M. W. Hansen (2012). "On the Use of Doppler Shift for Sea Surface Wind Retrieval From SAR". In: *IEEE Trans. on Geosci. and Remote Sensing* 50(7), pp. 2901–2909. DOI: 10.1109/TGRS.2011.2174998.

Munk, W. (2008). "An Inconvenient Sea Truth: Spread, Steepness, and Skewness of Surface Slopes". In: *Annu. Rev. Mar. Sci.* 1, pp. 377–415. DOI: n10.1146/annurev.marine.010908.163940.

Nouguier, F., A. Mouche, N. Rascle, B. Chapron, and D. Vandemark (2016). "Analysis of Dual-Frequency Ocean Backscatter Measurements at Ku- and Ka-Bands Using Near-Nadir Incidence GPM Radar Data". In: *IEEE Geoscience And Remote Sensing Letters* 31, pp. 2023–2245. DOI: 10.1109/LGRS.2016.2583198.

Nouguier, F., B. Chapron, F. Collard, A. Mouche, N. Rascle, F. Ardhuin, and X. Wu (2018). "Sea surface kinematics from near-nadir radar measurements". In: *IEEE Trans. on Geosci. and Remote Sensing* 56(10), pp. 6169–6179. DOI: 10.1109/TGRS.2018.2833200. URL: http://tiny.cc/SKIMonRG_NOUG.

Peureux, C. and F. Ardhuin (2016). "Ocean bottom pressure records from the Cascadia array and short surface gravity waves". In: *J. Geophys. Res.* 121, pp. 2862–2873. DOI: 10.1002/2015JC011580.

Peureux, C., A. Benetazzo, and F. Ardhuin (2018). "Note on the directional properties of meter-scale gravity waves". In: *Ocean Science* 14, pp. 41–52. DOI: 10.5194/os-14-41-2018.

Portilla, J., F. O. Torres, and J. Monbaliu (2009). "Spectral partitioning and identification of wind sea and swell". In: *J. Atmos. Ocean Technol.* 26, pp. 107–122.

Quilfen, Y. and B. Chapron (2019). "Ocean Surface Wave-Current Signatures From Satellite Altimeter Measurements". In: *Geophys. Res. Lett.* 216, pp. 253–261. DOI: 10.1029/2018GL081029.

Rascle, N. and F. Ardhuin (2013). "A global wave parameter database for geophysical applications. Part 2: model validation with improved source term parameterization". In: *Ocean Modelling* 70, pp. 174–188. DOI: 10.1016/j.ocemod.2012.12.001.

Rascle, N., J. Molemaker, L. Marié, F. Nouguier, B. Chapron, B. Lund, and A. Mouche (2017). "Intense deformation field at oceanic front inferred from directional sea surface roughness observations". In: *Geophys. Res. Lett.* 48, pp. 5599–5608. DOI: 10.1002/2017GL073473.

Rodríguez, E., A. Wineteer, D. Perkovic-Martin, T. Gál, B. W. Stiles, N. Niamsuwan, and R. R. Monje (2018). "Estimating Ocean Vector Winds and Currents Using a Ka-Band Pencil-Beam Doppler Scatterometer". In: *Remote Sensing* 4, p. 576. DOI: 10.3390/rs4000576.

Stewart, R. H. and J. W. Joy (1974). "HF radio measurements of surface currents". In: *Deep Sea Res.* 21, pp. 1039–1049.

Stopa, J. E., F. Ardhuin, and F. Girard-Ardhuin (2016). "Wave climate in the Arctic 1992-2014: seasonality and trends". In: *The Cryosphere* 10, pp. 1605–1629. DOI: 10.5194/tc-10-1605-2016.

Thomson, J., E. A. D'Asaro, M. F. Cronin, W. E. Rogers, R. R. Harcourt, and A. Shcherbina (2013). "Waves and the equilibrium range at Ocean Weather Station P". In: *J. Geophys. Res.* 118, pp. 595–5962. DOI: 10.1002/2013JC008837.

Tran, N., B. Chapron, and D. Vandemark (2007). "Effect of Long Waves on Ku-Band Ocean Radar Backscatter at Low Incidence Angles Using TRMM and Altimeter Data". In: *IEEE Geoscience And Remote Sensing Letters* 4(4), pp. 542–546. DOI: 10.1109/lgrs.2007.896329.

Vandemark, D., B. Chapron, J. Sun, G. H. Crescenti, and H. C. Graber (2004). "Ocean wave slope observations using radar backscatter and laser altimeters". In: *J. Phys. Oceanogr.* 34, pp. 2825–2842.

Vandemark, D., B. Chapron, H. Feng, and A. Mouche (2016). "Sea Surface Reflectivity Variation With Ocean Temperature at Ka-Band Observed Using Near-Nadir Satellite Radar Data". In: *IEEE Geoscience And Remote Sensing Letters* 13, pp. 510–514. DOI: 10.1109/lgrs.2016.2520823.

Walsh, E. J., M. L. Banner, C. W. Wright, D. C. Vandemark, B. Chapron, J. Jensen, and S. Lee (2008). "The Southern Ocean Waves Experiment. Part III: Sea Surface Slope Statistics and Near-Nadir Remote Sensing". In: *J. Phys. Oceanogr.* 38(3), pp. 670–685. DOI: 10.1175/2007JPO3771.1.

Walsh, E. J., D. C. Vandemark, C. A. Friehe, S. P. Burns, D. Khelif, R. N. Swift, and J. F. Scott (1998). "Sea Surface Ka-Band Doppler Measurements: Analysis and Model Development". In: *J. Geophys. Res.* 103(C6), pp. 12587–12601. DOI: 10.1029/97JC02443.

Welch, P. D. (1967). "The use of fast Fourier transform for the estimation of power spectra: a method based on time averaging over short, modified periodograms". In: *IEEE Trans. Audio and Electroacoustics* 15(2), pp. 70–73.

Yan, Q., J. Zhang, C. Fan, and J. Meng (2019). "Analysis of Ku- and Ka-Band Sea Surface Backscattering Characteristics at Low-Incidence Angles Based on the GPM Dual-Frequency Precipitation Radar Measurements". In: *Remote Sensing* 11(7), pp. 2023–2245. DOI: 10.3390/rs11070754.

Young, G. S., T. D. Sikora, and N. S. Winstead (2000). "Inferring Marine Atmospheric Boundary Layer Properties from Spectral Characteristics of Satellite-Borne SAR Imagery". In: *Mon. Weather Rev.* 128(5), pp. 1506–1520. DOI: 10.1175/1520-0493(2000)128<1506:IMABLP>2.0.CO;2.

Yurovsky, Y. Y., V. N. Kudryavtsev, S. A. Grodsky, and B. Chapron (2017). "Normalized Radar Backscattering Cross-section and Doppler Shifts of the Sea Surface in Ka-band". In: *Proceedings of the Progress In Electromagnetics Research Symposium (PIERS), May 2017, St Petersburg, Russia*. IEEE.

Yurovsky, Y. Y., V. N. Kudryavtsev, S. A. Grodsky, and B. Chapron (2019). "Sea Surface Ka-Band Doppler Measurements: Analysis and Model Development". In: *Remote Sensing* 11, p. 839. DOI: 10.3390/rs11070839.

Zhang, S. and D. T. Sandwell (2016). "Retracking of SARAL/AltiKa Radar Altimetry Waveforms for Optimal Gravity Field Recovery". In: *Marine Geology* 40(1), pp. 40–56. DOI: 10.1080/01490419.2016.1265032.